Phenanthraquinone modified carbon quantum dots covalent-grafted onto Cu-MOF for photocatalytic CO$_2$ reduction: Construction of dual-active sites and parallel charge channels based on the cooperation between photoexcitation and electron-entrap

Huiyang Ma [a,1], Tianyu Wang [a,1], Yifan Xu [a], Weiliang Shi [a], Ren Ma [a], Zhengqiang Xia [a,b,*], Qi Yang [a,b], Gang Xie [a,b], Sanping Chen [a,b,*]

[a] *Key Laboratory of Synthetic and Natural Functional Molecule Chemistry of Ministry of Education, College of Chemistry and Materials Science, Northwest University, Xi'an 710127, China*
[b] *Shaanxi Key Laboratory for Carbon Neutral Technology, Carbon Neutrality College (Yulin), Northwest University, Xi'an 710069, China*

ARTICLE INFO

ABSTRACT

How to coordinate the catalytic sites and the charge supply in CDs@MOFs hybrids to accelerate carriers transferring, suppress charge recombination and maximize charge transferring is a challenge. Here, the hybrid of PQ-CDs$_{6.67}$@Cu-TCA fabricated by Cu-TCA (TCA = 4,4',4''-nitrilotribenzoic acid) encapsulating 9,10-phenanthraquinone (9,10-PQ) modified carbon quantum dots (PQ-CDs), which was fully characterized and used for photocatalytic CO$_2$ reduction. Covalent-bonding of CDs with the paddle-wheel Cu structure and 9,10-PQ provides parallel electron pathways for accelerating electron transferring and minimum carrier recombination. PQ-CDs$_{6.67}$@Cu-TCA exhibited an excellent electron consumption rate (R_{ele}) of 393.98 μmol·g^{-1}·h^{-1} and a high CH$_4$ yield of 44.43 μmol·g^{-1}·h^{-1} with a selectivity of 90.22%, being far superior to most carbon materials/MOFs-based heterojunctions. Research evidences that through the parallel electron pathways, photon collection and transferring of PQ-CDs with optimal loading-amount meet chemical-producing Cu^{2+} and 9,10-PQ active centers, maximally improving electron utilization and suppressing the internal friction in PQ-CDs$_{6.67}$@Cu-TCA.

1. Introduction

To shift human dependence on fossil fuel to sustainable energy sources in the last decades, artificial photocatalysts such as carbon- [1], oxide- [2], and metal-based [3] heterojunctions/heterostructures, combining light capture centers and catalytic sites to generate effective chemical energy carriers, especially exploited for converting H$_2$O and CO$_2$ into solar fuels, have being developed [4].

Since MIL-125(Ti) was first reported for photocatalytic CO$_2$ reduction in 2012 [5], pristine metal−organic frameworks (MOFs) photocatalysts, such as UiO-66(Zr) and MIL-53/88B/101(Fe) have been successively explored [6,7]. Well known as a class of semiconductor-like crystalline porous materials, MOFs, constructed from organic linkers and metal clusters as nodes, have proven to be promising photocatalysis

[8–10]. However, compared with inorganic semiconductors, poor orbital overlap between organic linkers and metal-ions nodes in MOFs often restricts formation of continuous energy band, which renders most MOFs high optics bandgap energy and modest light harvesters that can merely harvest UV light or short wavelength visible light less than 500 nm, largely restraining their applications under the solar spectrum and therefore leading to low photocatalytic efficiency [11,12]. It is further emphasized that, in the absence of strong through-bond charge transport within most 3D MOFs, charge transferring proceeds predominantly *via* a short-range hopping mechanism to the final charge acceptors, while photoinduced charge separation occurs between neighboring guests, the framework or media reactants [13,14]. Besides, because the symmetry of the orbital of MOF and that of the ligand are not well-matched, the energy levels of most MOFs like UiO-66(Zr) are

not sufficiently arranged [15], resulting in electrons not being transferred over a long distance, thus exhibiting a poor conductive behavior. To conclude above, although MOF photocatalysts have seen substantial achievements in fuel production, they need to confront the challenges of their framework-determined mismatched distances and ill-suited photoactive nodes or linkers diverting energy and charges away from catalysis. To address the issues above, construction of MOF photocatalyst should meet the requirements to extent the light absorption of MOFs, improve ability of electron transferring and suppress charge recombination.

Reducing MOFs dimension to metal-organic layers is one of effective strategies to improve electrical conductivity while inevitably at the expense of stability, especially MOFs are originally intolerant to water/vapor, high temperature and strong electron beams [16,17]. Alternatively, taking full advantage of MOFs user-configurable flexibility and tunable pore environment, construction of MOF-based composites through encapsulating highly conductive materials is expected to integrate the advantages of individual components and overcome the disadvantages of poor electrical conductivity, resulting in synergistic effects and new possibilities [18,19].

Carbon quantum dots (CDs), a novel class of carbon nanomaterials with prominent fluorescence, exhibits broad UV–visible absorption profiles with n-π* and π-π* transitions and large π-conjugation systems composed by sp^2/sp^3 hybridized carbon atoms, endowing them with excellent photoelectronic conversion capability and high electrical conductivity [20,21]. Encapsulating low-cost and nontoxic CDs with adjustable size and surface functional groups into MOF cavities to contact as closely as possible with these metal sites, in principle, should be preference to improve the conductivity of MOFs in comparison with the method of loading conventional photosensitizers such as Ru(2, 2'-bipyridine)$_3^{2+}$, CdS, noble metal nanoparticles, etc [22]. Efforts have been made to develop CDs@MOFs photocatalysts integrating MOFs with CDs to improve the conductivity of MOFs and result in new user-friendly configurations [16]. In 2020, Li et al. reported a CDs@UiO-66-NH$_2$ composite by embedding CDs inside UiO-66-NH$_2$, showing a CO yield of 16.6 μmol·g^{-1}·h^{-1}, which was attributed that CDs as electron receptors and photosensitizers enhances conductivity [11]. CDs@NH$_2$-MIL-88B (Fe) nanohybrid exhibited an outstanding photocatalytic degradation tetracycline activity of 527 mol·min^{-1}·g^{-1} and recycling performance of 20 times reuse [23]. As the catalytic activity, selectivity and reactivity of the catalytic systems are readily affected by their environments, anchoring and confinement effects can result in improved or suppressed the catalytic performance [24–26]. As such, the connection pattern between MOF and CDs directly determines whether the charge generated by CDs reach the metal catalytic site within their intrinsic carrier lifetime [27,28]. It is a great challengeable to coordinate the catalytic sites and the charge transferring, and trade off the MOF porosity and the CDs loading amount in the CDs@MOFs hybrids to maximize the charge supply by CDs.

Herein, Cu-TCA was synthesized by incorporating 4,4′,4"-tricarboxylic triphenylamine (H$_3$TCA) and Cu^{2+}, and the activated Cu-TCA exposes unsaturated coordination Cu paddle-wheel structure acted as CO$_2$ conversion active centers. As expected, the single-component MOF lacks electrical conductivity and shows modest photocatalytic CO$_2$ reduction activity. Therewith, CDs was covalently grafted on Cu active centers in the paddle-wheel structure through carboxyl coordination. A series of CDs$_x$@Cu-TCA heterojunctions have been prepared. The covalent-bonding allows electrons transferring to Cu sites in the shortest distance, which overcomes inefficient ligand-to-metal charge transfer (LMCT) in Cu-TCA. The charge transfer impedance of CDs$_{6.73}$@Cu-TCA was minish to 31.13 Ω from 71.31 Ω. CDs$_{6.73}$@Cu-TCA displayed a good visible-light-driven CO$_2$ reduction performance with an electron consumption rate (R_{ele}) of 159.56 μmol·g^{-1}·h^{-1} and a selectivity of CO$_2$-to-CH$_4$ (S_{CH4}) of 56.76%. To minimize charge recombination, further investigate whether the photoexcited electrons produced by CDs are maximally transferred to the Cu sites, 9,10-phenanthraquinone (9,10-

PQ) molecule was chemically modified with the CDs *via* an acylation reaction. Due to the electron withdrawing effect, 9,10-PQ as the electron acceptor facilitates the electron transferring from CDs to the dicarbonyl site of PQ, providing parallel electron transferring pathways for the photocatalysis system. The existence of dual-active sites with parallel electron transferring pathways has enhanced charge separation ability of PQ-CDs$_{6.67}$@Cu-TCA and presented significant improving R_{ele} (393.98 μmol·g^{-1}·h^{-1}) and S_{CH4} (90.22%), which was 2.47-fold higher than that of CDs$_{6.73}$@Cu-TCA and superior to most reported carbon/MOFs-based photocatalysts. Fs-TAS, *in-situ* DRIFTS and DFT calculations also testified the parallel electron transferring pathways and the transformation path of CO$_2$ methanation on both 9,10-PQ and paddle-wheel Cu sites, 9,10-PQ stabilizing the intermediate CO* and lowering the rate-determining step energy barrier. Covalent grafting triggered a template effect of mutual support, and PQ-CDs$_{6.67}$@Cu-TCA exhibited robust stability.

2. Experimental section

2.1. Synthesis of CDs$_x$@Cu-TCA

Cu(NO$_3$)$_2$·3 H$_2$O (24.2 mg, 0.1 mmol) and H$_3$TCA (18.9 mg, 0.05 mmol) was ultrasound-dissolved in mixed solvent of MeOH and DMF (4.25 mL, $V:V$ = 1:16), to which aqueous solution (1.0 mL) of CDs (0.5, 1.0, 1.5, and 2.0 mg) was slowly injected. The mixed solution was transferred into a 25 mL Teflon-lined stainless-steel autoclave and kept for 72 h at 120 °C. After cooling to room temperature, the mixture was filtered to obtain precipitate, and the precipitate was washed with DMF three times. The precipitate has been soaking in MeOH for 48 hours, with MeOH being replaced every 6 hours. Finally, the product was dried in a vacuum at 60 °C for 24 h to obtain CDs$_{3.24}$@Cu-TCA, CDs$_{4.58}$@Cu-TCA, CDs$_{5.75}$@Cu-TCA, and CDs$_{6.73}$@Cu-TCA, respectively. The elemental analyses of the prepared samples are shown in Table S1.

2.2. Synthesis of PQ-CDs$_{6.67}$@Cu-TCA

The same as the synthesis of CDs$_x$@Cu-TCA, except replacing **CDs** with **PQ-CDs** (2.0 mg). The elemental analyses of the prepared sample are shown in Table S1.

2.3. Characterization

Powder X-Ray diffraction (PXRD) patterns were recorded on a Bruker D8 ADVANCE, using Cu Kα radiation (λ = 1.54056 Å). Fourier Transform infrared (FT-IR) spectra were recorded on a Bruker Tensor 27 spectrophotometer using KBr pellets in the range of 400–4000 cm^{-1}. Scanning electron microscopy (SEM) images were acquired on a Hitachi SU-8010 SEM. Transmission electron microscopy (TEM) images and energy-dispersive X-ray (EDX) spectra were performed on a FEI Talos F200X microscope operated at 200 kV. Ultraviolet photoelectron spectroscopy (UPS) measurements were performed on a Thermo Fisher ESCALAB Xi+ using a He Iα (21.22 eV) excitation line. UV–vis diffuse reflectance spectra (UV–vis-DRS) were obtained on a Shimadzu UV-3600Plus spectrophotometer using BaSO$_4$ as a reflectance standard. Elemental analyses were performed on a Vario EL III elemental analyzer and an Agilent 7900 ICP-MS. X-ray photoelectron spectrum (XPS) analyses were carried out on a PHI5000 Versa Probe III spectrometer with an Al-Kα (1486.6 eV) achromatic X-ray source. *In-situ* irradiation XPS were obtained from a JEOL JPS-9010MC electron spectrometer upon the light irradiation (λ = 400 ~ 800 nm). N$_2$ adsorption-desorption isotherms were recorded on Tristar 3020, and the surface areas were calculated using the Brunauer-Emmett-Teller (BET) equation. CO$_2$ adsorption-desorption isotherms were assessed on a JW-BK300C instruments. CO$_2$ temperature programmed desorption (CO$_2$-TPD) tests were conducted on a Micromeritics AutoChem II 2920 instrument. ^{1}HNMR spectra were recorded using a 400 MHz nuclear magnetic
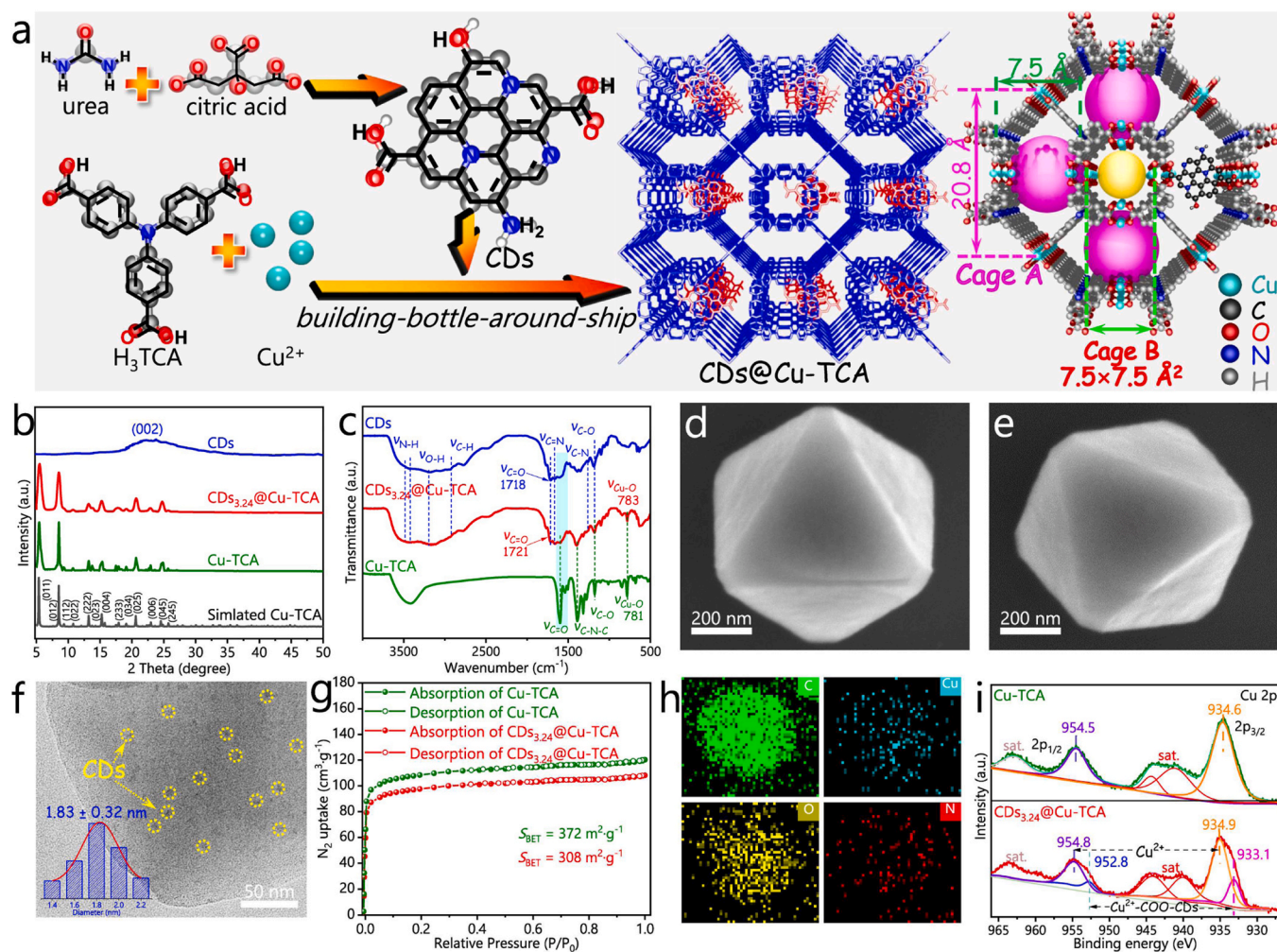
Fig. 1. (a) Schematic diagram of the preparation processes for CDs and CDs@Cu-TCA composites. (b) PXRD patterns and (c) FT-IR spectra of CDs, Cu-TCA and $CDs_{3.24}$@Cu-TCA. SEM images of (d) $CDs_{3.24}$@Cu-TCA and (e) Cu-TCA. (f) TEM image of $CDs_{3.24}$@Cu-TCA. (g) N_2 sorption-desorption isotherms of Cu-TCA and $CDs_{3.24}$@Cu-TCA. (h) EDX mapping of $CDs_{3.24}$@Cu-TCA. (i) High resolution XPS of Cu 2p for Cu-TCA and $CDs_{3.24}$@Cu-TCA.

resonance spectrometer (Bruker AV500, TMS as the internal standard). Room-temperature photoluminescence (PL) spectra and time-resolved photoluminescence (TRPL) decay dynamics spectra were detected on an Edinburgh instruments Ltd. FLSP920 fluorescence spectrometer. Transient-state surface photovoltage (TPV) spectra was obtained through a TPV system (PerfectLight PL-TPV), consisting of a Nd:YAG laser, Preamplifier, and 500 MHz oscilloscopes. *In-situ* diffuse reflectance infrared Fourier transform spectroscopy (DRIFTS) measurement was performed on a Bruker Vertex 70B within a mercury–cadmium–telluride (MCT) detector cooled by liquid nitrogen. The post-activated photocatalyst (5 mg) was evenly coated on the glass disc of 1 cm diameter and placed inside the photoreactor for monitoring reaction progress of photocatalytic CO_2 reduction. Next, the reactor was vacuum to remove the air and any adsorbed species, and high-purity CO_2 gas and water vapor was passed for 15 minutes inside the photoreactor. At last, the photoreactor was irradiated by visible-light using a white LED light (> 400 nm, 150 W).

2.4. Photocatalytic CO_2 reduction experiments

The photocatalytic CO_2 reduction experiments were conducted in a 50 mL closed reactor (TaiKang WCGF-50 mL) with a Xe lamp (Perfect Light PLS-SXE 300D, 300 W, 100 mW·cm^{-2}) containing a cut filter of 420 nm as a light source. The photocatalyst (5.0 mg) was added into a medium of MeCN, TEA, and H_2O (5 mL, *V/V/V*, 48/1/1). The reaction

system was degassed to get rid of the air inside, and the high-purity CO_2 gas was filled into the reactor with a pressure of 0.1 MPa. During the catalytic process, the system temperature was maintained at 25 °C by circulating cooling water. The collected gaseous products were detected using a gas chromatograph (FuLi GC9790 II) equipped with a flame ionization detector (FID) and a thermal conductivity detector (TCD). The liquid products and the isotope experiment were examined and carried out by a gas chromatography-mass spectrometer (Shimadzu GCMS-QP2010). The catalytic results were repeated three times with three batches of same catalysts to give more reliable data.

2.5. Other syntheses, characterizations and computational details

Syntheses of carbon quantum dots, 2-amino-9,10-phenanthrenedione, PQ-CDs and Cu-TCA; femtosecond transient absorption spectroscopy, photoelectrochemical, apparent quantum efficiency measurements and computational method are described in Supporting Information.

3. Results and discussion

3.1. Fabrication and structure of $CDs_{3.24}$@Cu-TCA composite

The CDs@Cu-TCA composite was constructed *via* a typical "building-bottle-around-ship" strategy (Fig. 1a). The carbon quantum dots (CDs)
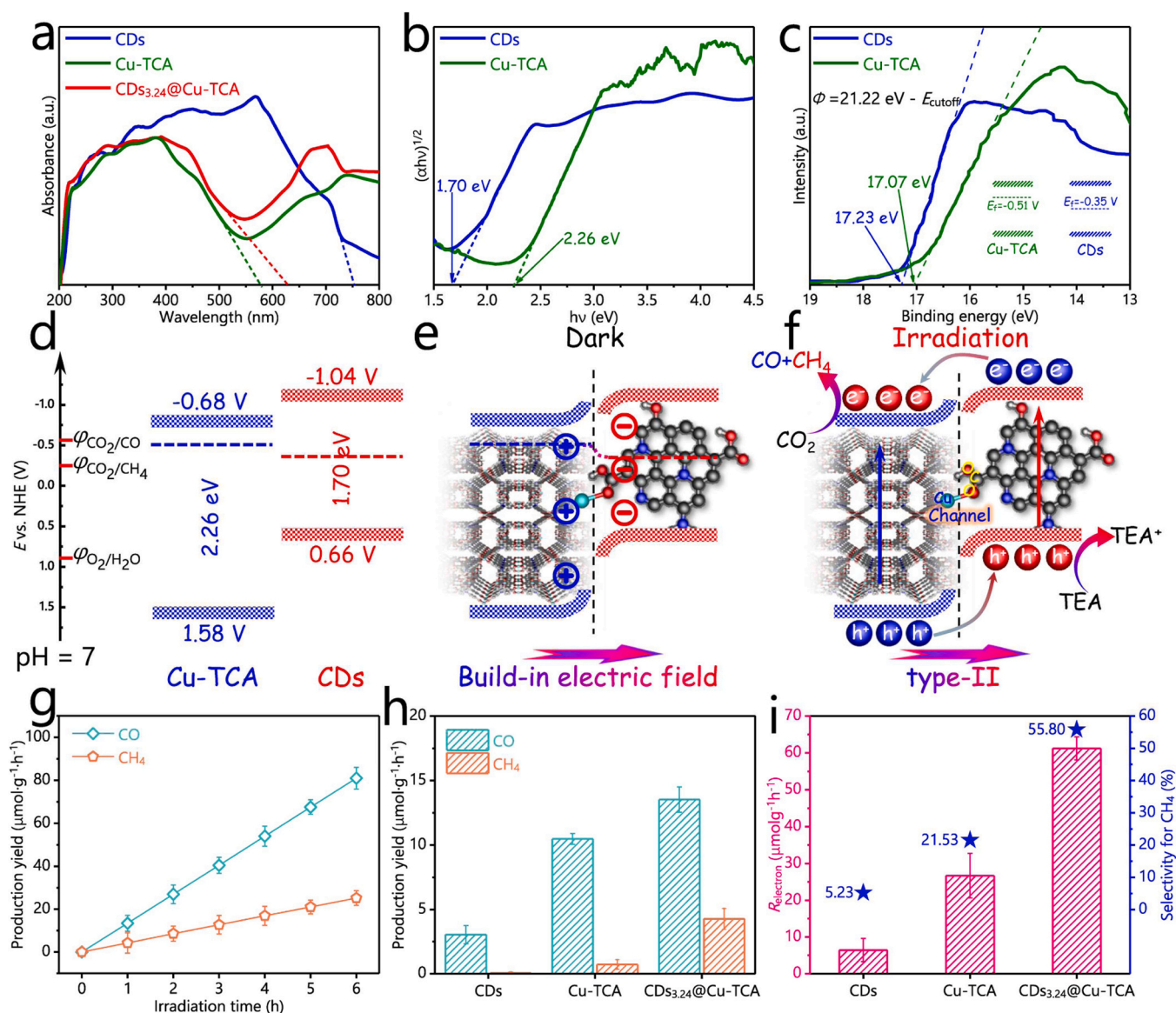
Fig. 2. (a) UV–vis-DRS of CDs, Cu-TCA, and CDs$_{3.24}$@Cu-TCA. (b) Tauc plots and (c) UPS of CDs and Cu-TCA. (d) The band structures of CDs and Cu-TCA. (e) The built-in electric fields and (f) type-II electron transfer mechanism in CDs$_{3.24}$@Cu-TCA heterojunction. (g) Time-dependent CO and CH$_4$ production over CDs$_{3.24}$@Cu-TCA as the photocatalyst. (h) R_{CO} and R_{CH4}, and (i) R_{ele} and S_{CH4} of CDs, Cu-TCA, and CDs$_{3.24}$@Cu-TCA.

was pre-synthesised according to the literature using citric acid and urea through a solvothermal method [29]. The structure resembles nitrogen-doped graphene with carboxyl and amino functional groups present at the edges, depicted in Fig. 1a. Its powder X-ray diffraction pattern (PXRD) shows a broad peak at 21.0°, which is attributed to the characteristic of graphitic structure in CDs (Fig. 1b) [30]. Its Fourier transform infrared (FT-IR) spectrum shows the vibration peaks at 3480, 3440, 3190, 2872, 1721, 1664 and 1600 ~ 1450 cm^{-1}, corresponding to the C(sp^2) conjugated aromatic structure and functional groups such as -COOH and -NH$_2$, etc. (Fig. 1c). The PXRD and FT-IR results match the literature [29,30], confirming the successful synthesis of CDs.

Dispersing as-prepared CDs in the precursor of Cu-TCA, CDs$_{3.24}$@Cu-TCA was synthesized after a solvothermal process. The PXRD pattern of CDs$_{3.24}$@Cu-TCA shows the diffraction peaks at 5.3, 8.5, 13.2 and 20.6°, agreeing well with the characteristic diffractions of (011), (012), (222) and (025) crystal facets for the simulated Cu-TCA skeleton (CCDC 841879), which indicates that the introduction of CDs does not interfere with the formation of Cu-TCA that is of a high crystallinity and phase purity (Fig. 1b). The characteristic diffractions of CDs are not reflect in

the PXRD pattern of CDs$_{3.24}$@Cu-TCA due to the low crystallinity of CDs [31]. In FT-IR spectrum of CDs$_{3.24}$@Cu-TCA, the characteristic vibration peaks of CDs including -COOH, -NH$_2$ and the conjugated aromatic structure etc. can be observed (Fig. 1c). In addition, the new strong peaks appeared at 1595 and 1320 cm^{-1} are attributed to the ν_{COO^-} and δ_{C-O} in the TCA^{3-} ligand of Cu-TCA [31]. Possibly owing to interaction between the carboxyl groups in CDs and the paddle-wheel Cu units, the characteristic peaks of $\nu_{C=O}$ and ν_{Cu-O} show a minor shift by 1–3 cm^{-1}. The PXRD and FT-IR tests above co-confirm the successful combination of CDs and Cu-TCA. As shown in Fig. 1d, the smooth octahedral morphology with grain size of ca. 500 nm for CDs$_{3.24}$@Cu-TCA can be observed in its scanning electron microscope (SEM) image, which is similar with that of Cu-TCA (Fig. 1e). There are no CDs observed on the surface of CDs$_{3.24}$@Cu-TCA, while they are encapsulated into the cavities of Cu-TCA which is demonstrated by the transmission electron microscopy (TEM) test. As shown in Fig. 1f, the uniform CDs with size of 1.83 ± 0.32 nm (the yellow circle areas) exist in the TEM image of CDs$_{3.24}$@Cu-TCA, which also indicates that CDs are encapsulated in the cavities.

Structural analysis discloses that Cu-TCA is composed of each TCA[3-] ligand connected three paddle-wheel binuclear Cu_2 units to form a non-interpenetrating 3D network (Fig. 1a). Each Cu^{2+} in the paddle-wheel Cu_2 units is coordinated with four symmetric-related oxygen atoms from four respective carboxylates and one axial H_2O molecule opposite to the Cu-Cu vector. The axially coordinated H_2O molecules are removed after the activation process, which has no effect in the framework structure. The overall framework consists of large truncated cubic "cages" delimited by 8 TCA[3-] ligands and 12 $Cu_2(O_2CR)_4$ paddle-wheel units. The 3D architecture involves two types of cavities: one has a larger window with diameter of about 7.5×20.8 Å (cage A) with co-ordinated unsaturated metal centers located in the same line, and the other with square shape has a small opening with approximate diameter of 7.5×7.5 Å (cage B). Therefore, CDs with diameter of 1.83 ± 0.32 nm can indeed be encapsulated into the cage A. Nitrogen adsorption-desorption isotherms were conducted at 77 K to further confirm the encapsulation of CDs into the cavities of Cu-TCA (Fig. 1g). CDs$_{3.24}$@Cu-TCA and Cu-TCA all exhibit typical type-I sorption isotherms with steep uptake at $P/P_0 = 0–0.02$, which corresponds to the microporous characteristics of Cu-TCA. The Brunauer-Emmett-Teller (BET) surface areas (S_{BET}) of CDs$_{3.24}$@Cu-TCA is decreased to 308.1 $m^2 \cdot g^{-1}$ compared with 372.6 $m^2 \cdot g^{-1}$ for Cu-TCA due to occupation of cavities by CDs. The decrement of S_{BET} indicates that CDs is encapsulated within cavities in line with the TEM image [32]. The elements of coexisting and uniformly distributed Cu, C, N and O in energy dispersive X-ray (EDX) mapping of CDs$_{3.24}$@Cu-TCA further confirm its successful preparation (Fig. 1h and S1). Subsequently, the precise weight percentages of CDs in CDs$_{3.24}$@Cu-TCA is determined to be 3.24% by inductively coupled plasma mass spectrometry (ICP-MS) analysis (Table S1).

For the sake of simplification, the paddle-wheel Cu_2 units without considering axial coordination water molecules are selected as the core structure of Cu-TCA, and merged with CDs to obtain a possible CDs@Cu-TCA heterojunction model, which is optimized by density functional theory (DFT) (Fig. S2a). As shown in Fig. 1a, CDs is encapsulated into the cavity of Cu-TCA and covalently connected with Cu^{2+} in the paddle-wheel Cu_2 units through the -COOH at the edges, with a bond distance d_{Cu-O} of 2.20 Å (Fig. S2b). To illustrate this, X-ray photoelectron spectroscopy (XPS) was used to analyze the distribution of electronic cloud for CDs$_{3.24}$@Cu-TCA. The survey XPS of CDs$_{3.24}$@Cu-TCA shows that the coexisting elements of Cu, C, N and O, which is consistent with the EDX mapping results (Figs. S3 and 1h). The high-resolution XPS of Cu 2p for CDs$_{3.24}$@Cu-TCA can be observed in two sets double-peaks at 954.8 and 934.9 eV as well as 952.8 and 933.1 eV that respond to Cu $2p_{1/2}$ and Cu $2p_{3/2}$ orbits (Fig. 1i). Therein, one double-peak at 954.8 and 934.9 eV is attributed to Cu^{2+} species of the pristine paddle-wheel Cu_2 node. As for the high-resolution Cu 2p spectrum of Cu-TCA, the signals of Cu^{2+} with the binding energies of 954.5 and 934.6 eV are also present, while another double-peak at low binding energies is nonexistent. Therefore, the double-peak at 952.8 and 933.1 eV in CDs$_{3.24}$@Cu-TCA can be reasonably assigned to the increase in electron cloud density of the partial Cu due to -COOH in CDs coordination to Cu in the paddle-wheel units. This result is consistent with the slight shift of the characteristic peaks of $\nu_{C=O}$ and ν_{Cu-O} in the FT-IR spectrum of CDs$_{3.24}$@Cu-TCA, which co-proves the covalent connection between CDs and Cu-TCA.

The optical absorption ability of CDs$_{3.24}$@Cu-TCA was checked by UV–vis diffuse reflectance spectroscopy (UV–vis-DRS). Cu-TCA displays broad visible light adsorption with an edge at 577 nm and a band centred around 737 nm, which is attributed to the ligand-to-metal charge transfer from the TCA[3-] to the paddle-wheel Cu_2 units and the d-d transition of the Cu^{2+} octahedral complex (Fig. 2a) [33]. The introduction of CDs redshifts the absorption edge to 627 nm and jointly determine the wide-band solar energy utilization of CDs$_{3.24}$@Cu-TCA. Based on UV–vis DRS, the Tauc plots of Cu-TCA and CDs were drawn according to the Kubelka-Munk formula [34]. Their band gaps (E_g) are determined to be 2.26 and 1.70 eV, respectively (Fig. 2b). Both Cu-TCA and CDs are corroborated to be n-type semiconductors due to their positive slope of

the Mott-Schottky plots, and their conduction band minimums (E_{CB}) are estimated to be -0.68 and -1.04 V (Fig. S4). According to the formula $E_{VB} = E_g - E_{CB}$, their valence band maximums (E_{VB}) are calculated to be 1.58 and 0.66 V. The Fermi levels (E_F) of Cu-TCA and CDs are measured to be -0.51 and -0.35 V by ultraviolet photoelectron spectroscopy (UPS) according to the formula $\Phi = h\nu - E_{cutoff}$, where $h\nu$ is the incident photon energy (21.22 eV) and E_{cutoff} represents the cutoff energy of secondary electrons (Fig. 2c). The standard reduction potentials of CO_2/CH_4, CO_2/CO and O_2/H_2O as well as the band structures of Cu-TCA and CDs are summarized in Fig. 2d.

Cu-TCA and CDs exhibit staggered-band structure, implying that the composite CDs$_{3.24}$@Cu-TCA forms a heterojunction. Because of the E_F of Cu-TCA is higher than that of CDs, upon the formation of the CDs@Cu-TCA heterojunction, at the heterointerface, the electrons on Cu-TCA side will spontaneously flow to CDs due to the lower work function (Φ) of Cu-TCA (3.99 eV) than that of CDs (4.15 eV) and the E_F resonance effect (Fig. 2e). This leads to the change of the electron cloud density of atoms in CDs@Cu-TCA, which is reflected in the XPS. Due to the presence of C, N, and O elements in both CDs and Cu-TCA, it is difficult to accurately distinguish these elements in the high-resolution spectrum of CDs$_{3.24}$@Cu-TCA. Only Cu-TCA contains Cu, so it makes sense to judge the flow of electrons from the change in the binding energy of the Cu element. In the high-resolution XPS of Cu 2p for Cu-TCA, the orbital binding energies of $2p_{1/2}$ and $2p_{3/2}$ at 954.5 and 934.6 eV, are the characteristic of Cu^{2+} (Fig. 1i). In the Cu 2p spectrum of CDs$_{3.24}$@Cu-TCA, the binding energy of Cu^{2+} (954.8 and 934.9 eV) undergoes a positive shift of 0.3 eV, indicating a decrease in electron cloud density of the partial Cu atoms in CDs$_{3.24}$@Cu-TCA caused by electron transferring from Cu-TCA to CDs.

As presented, the electropositivity of Cu-TCA side interface and the electronegativity of CDs side interface result in generation of built-in electric fields with a direction from Cu-TCA to CDs (Fig. 2e). Driven by the built-in electric fields, upon irradiation, electrons are transferred from CDs to Cu-TCA and the electrons and holes are ultimately be aggregated at the CB of Cu-TCA and at the VB of CDs, respectively, following the charge transferring mechanism of typical type-II heterojunction (Fig. 2f). The photo-inducing electron-transferring from CDs to Cu-TCA has further been experimentally confirmed by in-$situ$ irradiation XPS (ISI-XPS) analysis (Fig. 4g). Upon irradiation, the $2p_{1/2}$ and $2p_{3/2}$ orbital binding energies of Cu^{2+} in CDs$_{3.24}$@Cu-TCA (954.4 and 934.5) are negatively shifted by 0.4 eV compared to those in dark (954.8 and 934.9 eV), which clearly verified the type-II charge transferring mechanism for CDs$_{3.24}$@Cu-TCA. The sufficiently negative E_{CB} of Cu-TCA indicates its thermodynamic capability for photo-reducing CO_2 to CO or CH_4. Additionally, in type-II heterojunction, the carriers experience spatial separation and enrichment, which delays recombination of photogenerated electrons and holes, accelerates the overall charge transferring efficiency, and promotes the photocatalytic CO_2 reduction reaction.

To evaluate the photocatalytic efficiency, the pCO$_2$RR performance of the CDs$_{3.24}$@Cu-TCA heterojunction was investigated and performed in a CO_2-saturated MeCN/H$_2$O solution with TEA as a hole sacrificial agent upon irradiation under a 300 W Xe lamp. Under the optimized reaction conditions (1 mg·mL^{-1} catalyst, 5 mL MeCN/TEA/H$_2$O $V:V:V =$ 48:1:1, Table S2), CO and CH_4 are detected as the carbonous products for all as-synthesized samples through gas chromatography (Fig. S5a). No H_2 and liquid products are detected for all the evaluated photocatalytic systems. Under the identical conditions, CO and CH_4 aren't detected in a series of control experiments: without light, catalyst, CO_2, or H_2O (Fig. S5b). Due to the thermodynamic inability of CDs ($E_{VB} = 0.66$ V) to oxidize H_2O to O_2 ($\varphi = 0.81$ V), no products are detected without the addition of TEA (Table S2) [35]. Additionally, the ^{13}C isotope experiment was performed to confirm the carbon source of the reaction by mass spectrometry (MS), and the signal peaks at $m/z = 17$ ([13]CH$_4$) and 29 ([13]CO), originating from the used [13]CO$_2$, could be detected, clearly verifying that the carbonaceous products (CO and CH_4)
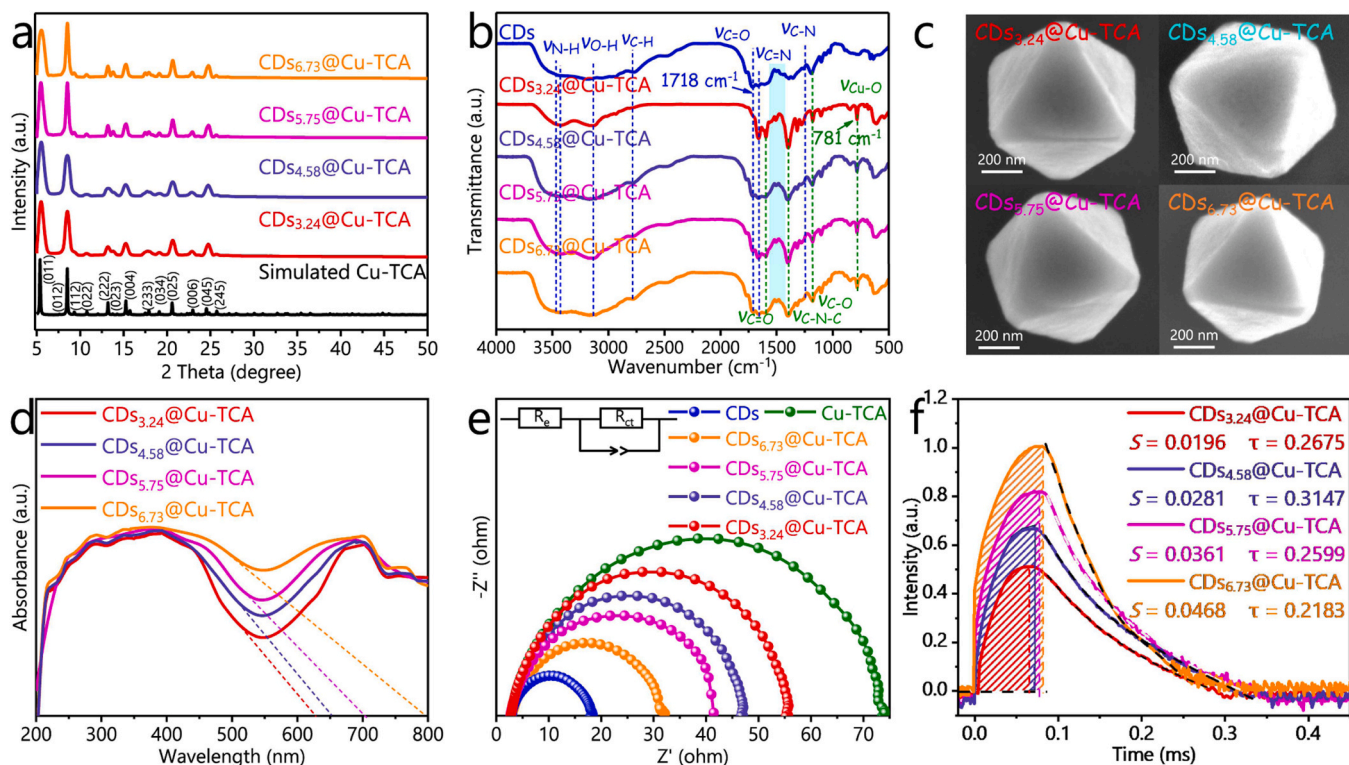
Fig. 3. (a) PXRD patterns, (b) FT-IR spectra, (c) SEM images and (d) UV–vis-DRS of CDs$_x$@Cu-TCA. (e) EIS Nyquist plots of CDs, Cu-TCA, and CDs$_x$@Cu-TCA. (f) TPV spectra of CDs$_x$@Cu-TCA.

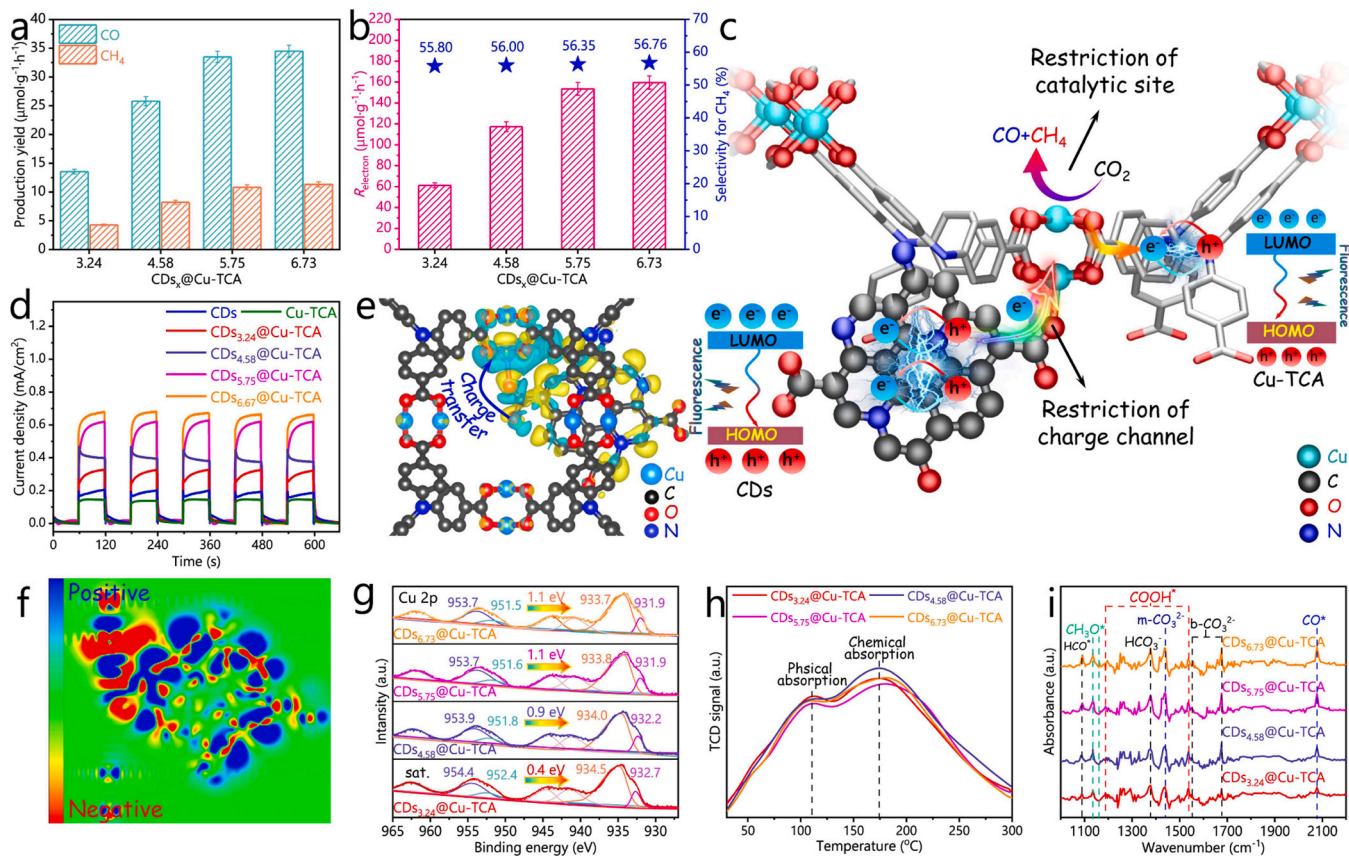**Fig. 4.** (a) R_{CO} and R_{CH4}, and (b) R_{ele} and S_{CH4} of CDs$_x$@Cu-TCA. (c) Schematic diagram of charge internal friction in CDs$_x$@Cu-TCA. (d) The *i-t* curves of CDs, Cu-TCA, and CDs$_x$@Cu-TCA. (e) The 3D charge density difference and (f) the planar charge density diagram of cross-section in CDs$_x$@Cu-TCA. (g) High resolution ISI-XPS of Cu 2p, (h) CO$_2$-TPD and (i) *in-situ* DRIFTS for CDs$_x$@Cu-TCA.

are indeed generated from the photocatalytic reduction of CO_2 (Fig. S6).

The productions of CO and CH_4 increase almost linearly during the continuous irradiation over $CDs_{3.24}@Cu$-TCA as the photocatalyst, resulting in the CO and CH_4 yields of 111.75 and 35.56 μmol·g^{-1} after 6 h of reaction (Fig. 2g). The highest hourly yields for CO (R_{CO}, 19.65 μmol·g^{-1}·h^{-1}) and CH_4 (R_{CH4}, 6.67 μmol·g^{-1}·h^{-1}) were detected at 2 hours of irradiation, thus the subsequent reaction duration was controlled at 2 hours (Fig. 2h and Table S2). Its electron consumption rate ($R_{ele} = 8R_{CH4} + 2R_{CO}$) is 92.56 μmol·g^{-1}·h^{-1} with CH_4 selectivity (S_{CH4}) of 58.62%, which is 4.3- and 17.7-fold higher than that of Cu-TCA (21.53 μmol·g^{-1}·h^{-1}) and CDs (5.24 μmol·g^{-1}·h^{-1}), respectively (Fig. 2i). The enhancement of catalytic activity benefits from the type-II electron transferring mechanism of $CDs_{3.24}@Cu$-TCA heterojunction.

Considering that CDs, as electron supplier in $CDs_{3.24}@Cu$-TCA heterojunction, determines the enrichment of electrons in the CB of Cu-TCA, increasing the proportion of CDs in the heterojunction may enhance the electron supply and catalytic performance. $CDs_x@Cu$-TCA ($x = 4.58$, 5.75 and 6.73%) heterojunctions with three greater CDs component proportions were prepared by augmenting CDs quantities in the synthetic process (Table S1). Their PXRD patterns match well with Cu-TCA, and there are no extra peaks observed, indicating the high phase purity and crystallinity of the heterojunctions (Fig. 3a). The FT-IR spectra of $CDs_x@Cu$-TCA are displayed in Fig. 3b, the structural units of CDs, including -C≡O, -OH, and -NH_2, etc., exhibit characteristic vibration peaks in increased intensity with greater CDs component proportions, which correlates with the results from ICP-MS (Table S1). The SEM images of $CDs_x@Cu$-TCA demonstrate uniform octahedral morphology and grain sizes that are consistent with $CDs_{3.24}@Cu$-TCA, which reveals that CDs are encapsulated within the cavities of Cu-TCA for all $CDs_x@Cu$-TCA heterojunctions (Fig. 3c). Besides, a gradual enhancement of visible light absorption in the range of 403–711 nm, attributed to the increasement of CDs content, can be observed from their UV–vis-DRS, which is ascribed to the n(π) → π* transitions and the pyridinic-N absorption in CDs (Fig. 3d) [36].

As can be seen in electrochemical impedance spectra (EIS), the introduction of CDs significantly improves the conductivity of Cu-TCA, the charge transfer impedances of $CDs_x@Cu$-TCA decrease to 54.73, 45.12, 41.25 and 31.13 Ω with increasing the component proportion of CDs, respectively (Fig. 3e and Table S3), demonstrating the covalent-channel allows electrons to reach Cu sites in the shortest distance, which overcomes inefficient LMCT of the Cu-TCA and improves the conductivity. The electron supply capacity of $CDs_x@Cu$-TCA was quantificationally evaluated by transient-state surface photovoltage (TPV) spectroscopy. The amounts of maximum charge extraction (S) of $CDs_x@Cu$-TCA are measured to be 0.0196, 0.0281, 0.0361 and 0.0468 ×10^{-6} V·s, indicating the increase of the component proportion of CDs indeed improves the electron supply for heterojunction (Fig. 3f). Subsequently, the photocatalytic CO_2 reduction performance of $CDs_x@Cu$-TCA heterojunctions was evaluated under the same conditions as $CDs_{3.24}@Cu$-TCA. As anticipated, $CDs_{4.58}@Cu$-TCA demonstrates a notable enhancement in catalytic activity towards R_{CH4}, R_{CO} and R_{ele} with 9.71, 27.8 and 133.28 μmol·g^{-1}·h^{-1}, respectively, which is attributed to that the elevated component proportion of CDs increases the electron supply to the heterojunction (Fig. 4a and b). However, the R_{ele} of $CDs_{5.75}@Cu$-TCA with a further increase in the component proportion of CDs is only improved to 147.48 μmol·g^{-1}·h^{-1}, and $CDs_{6.73}@Cu$-TCA is even barely improved (147.56 μmol·g^{-1}·h^{-1}). As illustrated in Fig. 4d, the transient photocurrent response (i-t) curves of $CDs_{5.75}@Cu$-TCA and $CDs_{6.73}@Cu$-TCA show the highest similar average photocurrent density of 0.6455 μA·cm^{-3}, which is consistent with the catalytic results. Although the increased proportion of CDs improves the charge supply, the overall charge separation performance of the heterojunction appears to be limited.

The mismatching between electron supply and catalytic activity may be caused by the electronic internal friction of the heterojunction limiting the charge separation (Fig. 4c), which can be reflected in

photoluminescence (PL) and time-resolved photoluminescence (TRPL) decay spectroscopy. At an excitation wavelength of 400 nm, the PL emission spectra of Cu-TCA, CDs, and $CDs_x@Cu$-TCA are obtained, exhibiting their fluorescence signals with maximum emission wavelengths at 518.5, 532.3 and 525.8 nm, respectively (Fig. S7a) [37]. The PL intensity increases with the order of $CDs_{4.58}@Cu$-TCA < $CDs_{3.24}@Cu$-TCA < $CDs_{5.75}@Cu$-TCA < $CDs_{6.73}@Cu$-TCA. Their TRPL spectra also show the same trend, with average PL lifetimes (τ_{av}) of 10.5374, 10.2581, 9.9412 and 9.8692 ns (Fig. S7b and Table S4). Therefore, even if $CDs_{5.75}@Cu$-TCA and $CDs_{6.73}@Cu$-TCA with a higher proportion of CDs enhance electron supply, severe electronic internal friction affects the charge separation of heterojunctions and limits their catalytic performance.

To gain insight into the reasons for the electron internal depletion in $CDs_{6.73}@Cu$-TCA, the 3D charge density difference of $CDs@Cu$-TCA is obtained by DFT calculation, where the blue and yellow regions represent electron density accumulation and depression, respectively (Fig. 4e). Apparently, the intense charge exchange occurs between the paddle-wheel Cu_2 unit and CDs along Cu-O charge channel, resulting in the negative and positive charges are enriched on the paddle-wheel Cu_2 unit and CDs, respectively. However, a significant red region is still present in the planar deformation charge density (DCD) of the dipole plane for CDs (Fig. S8), suggesting that the electrons are not fully transferred to the paddle-wheel Cu_2 unit, possibly due to the Cu-O channel charge transport reaching its bottleneck (Fig. 4f). Besides, the ISI-XPS of $CDs_x@Cu$-TCA are tested to further demonstrate the result above. As illustrated in Fig. 4g, the Cu 2p orbital binding energies of $CDs_{3.24}@Cu$-TCA at 954.4, 952.4, 934.5 and 932.7 eV upon irradiation, respectively, are negatively shifted by 0.4 eV compared to those in the dark (Fig. 1i), which is because of electrons from the CDs transferring to the paddle-wheel Cu_2 units and following the type-II heterojunction mechanism. The negatively shift values of the Cu 2p orbital binding energies for $CDs_{4.58}@Cu$-TCA and $CDs_{5.75}@Cu$-TCA increase to 0.9 and 1.1 eV, respectively. The negatively shift values for $CDs_{6.73}@Cu$-TCA don't increase any further, which suggests that the electron transferring from the CDs to the paddle-wheel Cu_2 units in $CDs_{5.75}@Cu$-TCA and $CDs_{6.73}@Cu$-TCA has reached its upper limit. Hence, additional CDs-created electrons can no longer be availably supplied to the paddle-wheel Cu_2 units (Fig. 4c).

The CO_2 uptake-adsorption-activation-conversion were monitored through CO_2 adsorption-desorption isotherms, CO_2 temperature programmed desorption (CO_2-TPD) and *in-situ* diffuse reflectance infrared Fourier transform spectroscopy (DRIFTS). The CO_2 adsorption-desorption isotherms show that $CDs_x@Cu$-TCA exhibits the CO_2 uptakes of 90.48 ~ 106.26 cm^3·g^{-1} at 298 K under 1 bar, respectively, maintaining the close CO_2 adsorption capacity (Fig. S9). Four $CDs_x@Cu$-TCA exhibit the similar CO_2-TPD curves with two desorption peaks centered near 110.2 and 174.5 °C, corresponding to the physisorption and chemisorption of CO_2 for the heterojunctions (Fig. 4h). Apparently, the increase in the component proportions of CDs don't improve the CO_2 uptake-adsorption properties of the heterojunctions, which is because the main component of adsorbed CO_2 is Cu-TCA and the content of CDs is less variable (3.24 ~ 6.73%). Besides, in the *in-situ* DRIFTS analysis of $CDs_x@Cu$-TCA heterojunctions, the diffuse reflection peaks of HCO* (at 1792 cm^{-1}), CH_3O* (at 1134 and 1159 cm^{-1}), HCO_3* (at 1376 cm^{-1}), COOH* (at 1187 and 1537 cm^{-1}), monodentate carbonate (m-CO_3^{2-}, at 1441 cm^{-1}), bidentate carbonate (b-CO_3^{2-}, at 1552 and 1676 cm^{-1}) and CO* (2077 cm^{-1}) are recorded, which is the reaction intermediates during photocatalytic CO_2 reduction (Fig. 4i). Meanwhile, the peaks intensities of intermediates increase with increasing the component proportions of CDs in $CDs_{3.24}@Cu$-TCA, $CDs_{4.58}@Cu$-TCA and $CDs_{5.75}@Cu$-TCA, indicating that more electrons are bound to CO_2 for the catalytic reaction and resulting in a gradually enlarged concentration of intermediates. Notably, the concentrations of intermediate no longer increase for $CDs_{6.73}@Cu$-TCA, which implies that the conversion of CO_2 reaches a state of saturation or excess (Fig. 4c), in line with the
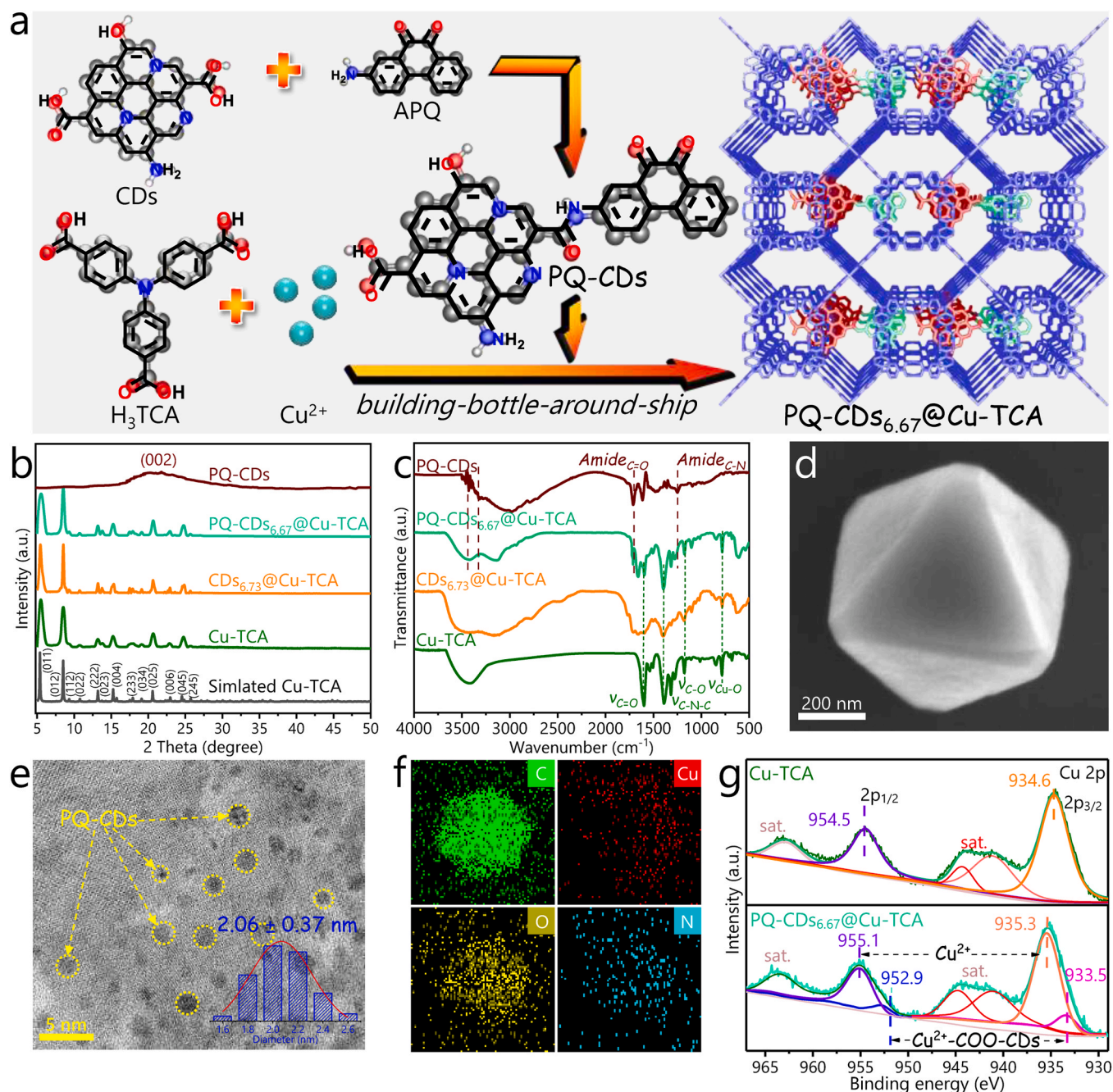
Fig. 5. (a) Schematic diagram of the preparation processes for PQ-CDs and PQ-CDs$_{6.67}$@Cu-TCA composite. (b) PXRD patterns and (c) FT-IR spectra of PQ-CDs, Cu-TCA, CDs$_{6.73}$@Cu-TCA, and PQ-CDs$_{6.67}$@Cu-TCA. (d) SEM image, (e) TEM image and (f) EDX mapping of PQ-CDs$_{6.67}$@Cu-TCA. (g) High resolution XPS of Cu 2p for Cu-TCA and PQ-CDs$_{6.67}$@Cu-TCA.

catalytic results (Fig. 4a).

3.2. Establishment of dual-catalytic site and parallel charge transferring pathways

Considering that electron transfer *via* the Cu-O charge channel and the paddle-wheel Cu$_2$ units catalytic site reach their upper limit for charge transfer and CO$_2$ conversion, charge internal friction will certainly restrict the catalytic performance of the CDs$_x$@Cu-TCA heterojunctions. Based on the electron-rich donor of CDs with a large π-conjugation system, introducing another catalytic site of electron-deficient acceptor on CDs to shunt excess photogenerated electrons would create a parallel intramolecular charge transferring pathway that

could efficiently utilize the abundance of electrons generated by CDs and mitigate charge internal friction [38,39]. 9,10-phenanthraquinone (9,10-PQ) is an excellent metal-free catalytic functional group with strong electron withdrawing effect and modifiability [40], and it is suitable for covalent grafting with CDs and would serve as a new catalytic site for accepting electrons, which may further improve the conversion yield of CO$_2$.

To illustrate understanding, 2-amino-9,10-phenanthrenedione (APQ) was linked on CDs *via* an amide bond and acylation reaction, and the successful synthesis of PQ-modificatory CDs (PQ-CDs) was identified by FT-IR and XPS (Fig. S10 and S11). Subsequently, CDs was replaced with PQ-CDs to combine with Cu-TCA, and the PQ-CDs$_{6.67}$@Cu-TCA heterojunction was synthesized with the same method
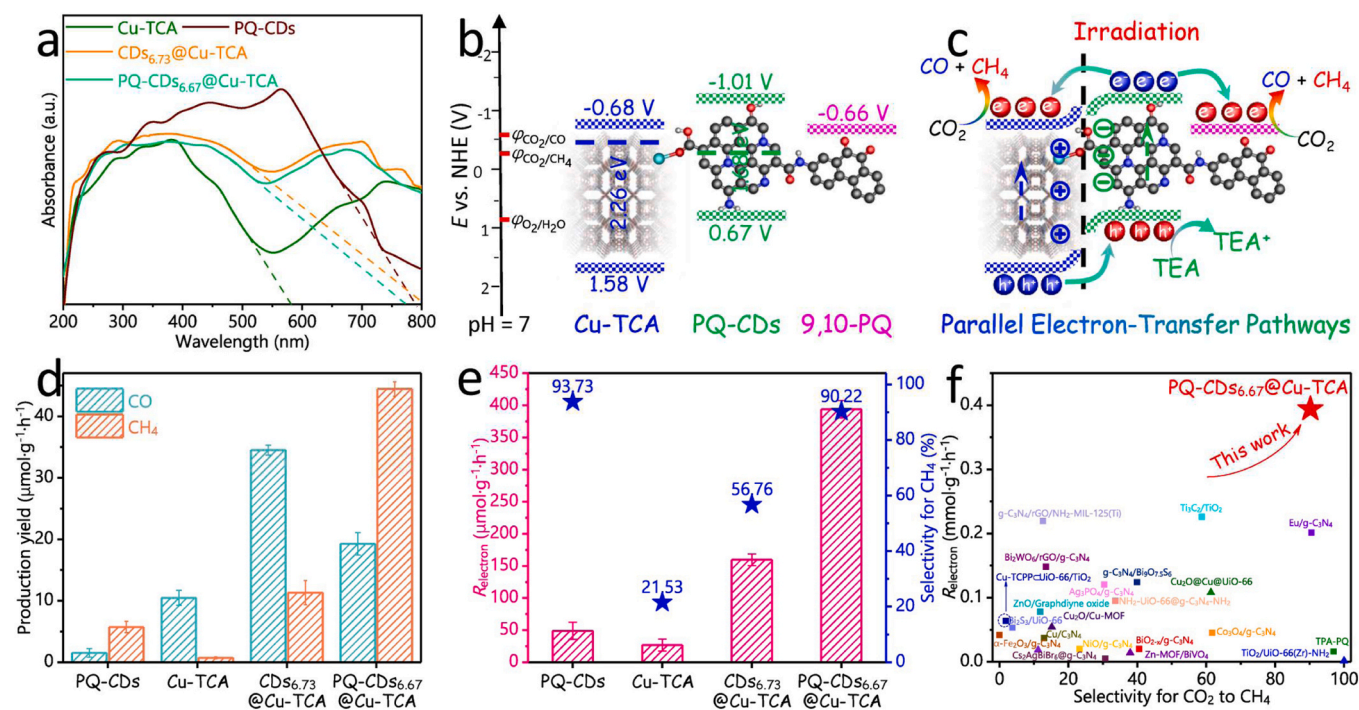
Fig. 6. (a) UV–vis-DRS of PQ-CDs, Cu-TCA, and CDs$_{6.73}$@Cu-TCA and PQ-CDs$_{6.67}$@Cu-TCA. (b) The band structures of PQ-CDs and Cu-TCA, as well as the LUMO energy level of 9,10-PQ. (c) The electron transfer mechanism with parallel electron-transfer pathways in PQ-CDs$_{6.67}$@Cu-TCA. (d) R_{CO} and R_{CH4}, and (e) R_{ele} and S_{CH4} of PQ-CDs, Cu-TCA, CDs$_{6.73}$@Cu-TCA and PQ-CDs$_{6.67}$@Cu-TCA. (f) Catalytic performance comparison of PQ-CDs$_{6.67}$@Cu-TCA and some reported carbon material- and MOFs-based heterojunction photocatalysts.

(Fig. 5a). Its component proportion is very close to that of the CDs$_{6.73}$@Cu-TCA by strict controlling the raw material input and determined through ICP-MS (Table S1). PXRD pattern and FT-IR spectrum confirm the formation and phase purity of the PQ-CDs$_{6.67}$@Cu-TCA heterojunction photocatalyst (Figs. 5b and 5c). Particularly, two strong vibration peaks emerged at 1590 and 1260 cm^{-1} in its FT-IR spectrum, can be assigned to the characteristic vibration of II band ($\nu_{C=O}$) and III band (δ_{C-N}) for carbonyl amide group. The SEM image of PQ-CDs$_{6.67}$@Cu-TCA shows the regular and smooth octahedral morphology with size of ca. 500 nm (Fig. 5d). As can be seen in Fig. 5e, the PQ-CDs with size of 2.06 ± 0.37 nm encapsulated by Cu-TCA are clearly observed in the TEM image (circled in yellow). The uniformly distributing elements of Cu, C, N and O are coexisted and can be observed in its EDX mapping (Fig. 5f). Its S_{BET} is calculated to be 286.4 m^{2}g^{-1} from the N$_2$ adsorption desorption isotherm, indicating the cavity of Cu-TCA is occupied by PQ-CDs (Fig. S12). The results above confirm the successful preparation of PQ-CDs$_{6.67}$@Cu-TCA heterojunction, and PQ-CDs are introduced into the cavity of Cu-TCA. In the high-resolution XPS of Cu 2p for PQ-CDs$_{6.67}$@Cu-TCA, the existence of the strong electronegativity Cu^{2+} with binging energies of 952.9 and 933.5 eV also verifies the coordination of -COOH in CDs and to Cu in paddle-wheel units (Fig. 5g). Compared with Cu-TCA, the binding energies of Cu^{2+} for PQ-CDs$_{6.67}$@Cu-TCA are negatively shifted by 0.6 ～ 0.7 eV, illustrating electronic transferring from PQ-CDs to Cu-TCA.

PQ-CDs$_{6.67}$@Cu-TCA shows similar light-harvesting capacity with almost full visible light region to CDs$_{6.73}$@Cu-TCA (Fig. 6a). Meanwhile, the highly conjugated π-π stacking structure endows PQ-CDs$_{6.67}$@Cu-TCA with high conductivity and the charge transfer impedance is reduced to 24.24 Ω from 71.31 Ω (for Cu-TCA) (Fig. S13). Tauc plot, Mott-Schottky plot and UPS tests show that the modifying for CDs don't affect the intrinsic band structure of PQ-CDs significantly (E_g, E_{CB}, E_F and E_{VB} are determined to be 1.68 eV, −1.01, −0.37 and 0.67 V, respectively) and PQ-CDs$_{6.67}$@Cu-TCA have almost the same built-in electric field and type-II heterojunction mechanism with CDs$_{6.73}$@Cu-TCA (Fig. S14-S16). Particularly, the LUMO energy level (E_{LUMO}) of 9,10-PQ

is measured to be −0.66 V by cyclic voltammetry (Fig. S17), which is right for transferring remining electrons from CDs to 9,10-PQ (Figs. 6b and 6c). Thus, the parallel electron transferring pathways of electrons from CDs to Cu-TCA and from the CDs to the 9,10-PQ functional group coexist in PQ-CDs$_{6.67}$@Cu-TCA. Furthermore, the suitable energy level indicates that 9,10-PQ has the thermodynamic ability to reduce CO$_2$ to CH$_4$ and CO.

The photocatalytic CO$_2$ reduction activity of PQ-CDs$_{6.67}$@Cu-TCA was evaluated under the same catalytic system as CDs$_x$@Cu-TCA. The R_{CH4} and R_{CO} are measured to be 44.43 and 19.27 μmol·g^{-1}·h^{-1} (Fig. 6d). The R_{ele} is calculated to be 393.98 μmol·g^{-1}·h^{-1}, which is 2.47-fold higher than that of CDs$_{6.73}$@Cu-TCA (159.56 μmol·g^{-1}·h^{-1}) (Fig. 6e). Eminently, its S_{CH4} increases to 90.22%, which is attributed to the high conversion reactivity of CO$_2$ methanation for PQ-CDs (S_{CH4} = 93.73%). These excellent performances are superior to most reported carbon/MOFs-based heterojunction photocatalysts (Fig. 6f and Table S5). The apparent quantum efficiency (AQE) upon irradiation of 700 nm monochromatic light for PQ-CDs$_{6.67}$@Cu-TCA is tested to be 3.35% (Fig. S18), which is also higher than those of some carbon-based photocatalysts (Table S6) [41–44]. Besides, the catalytic durability and stability of PQ-CDs$_{6.67}$@Cu-TCA was examined by cycles experiments. PQ-CDs$_{6.67}$@Cu-TCA still retains the original R_{ele} of 95.4% (376.0 μmol·g^{-1}·h^{-1}) after 30 cycles (Fig. S19). Improved stability is due to the mutual support between PQ-CDs and Cu-TCA and the resulting template effect. The PXRD pattern, FT-IR spectrum and ICP-MS of the reclaimed PQ-CDs$_{6.67}$@Cu-TCA retain the characteristic peaks and proportions of two components, which indicates that the skeleton integrity and structural units of PQ-CDs and Cu-TCA are well maintained after the photocatalytic CO$_2$ reduction reaction (Fig. S20, S21 and Table S1). The morphology of smooth octahedra is well maintained in PQ-CDs$_{6.67}$@Cu-TCA after 30 cycles of photocatalytic experiments (Fig. S22). The results above confirm that PQ-CDs$_{6.67}$@Cu-TCA possesses excellent durability and stability during photocatalytic process.

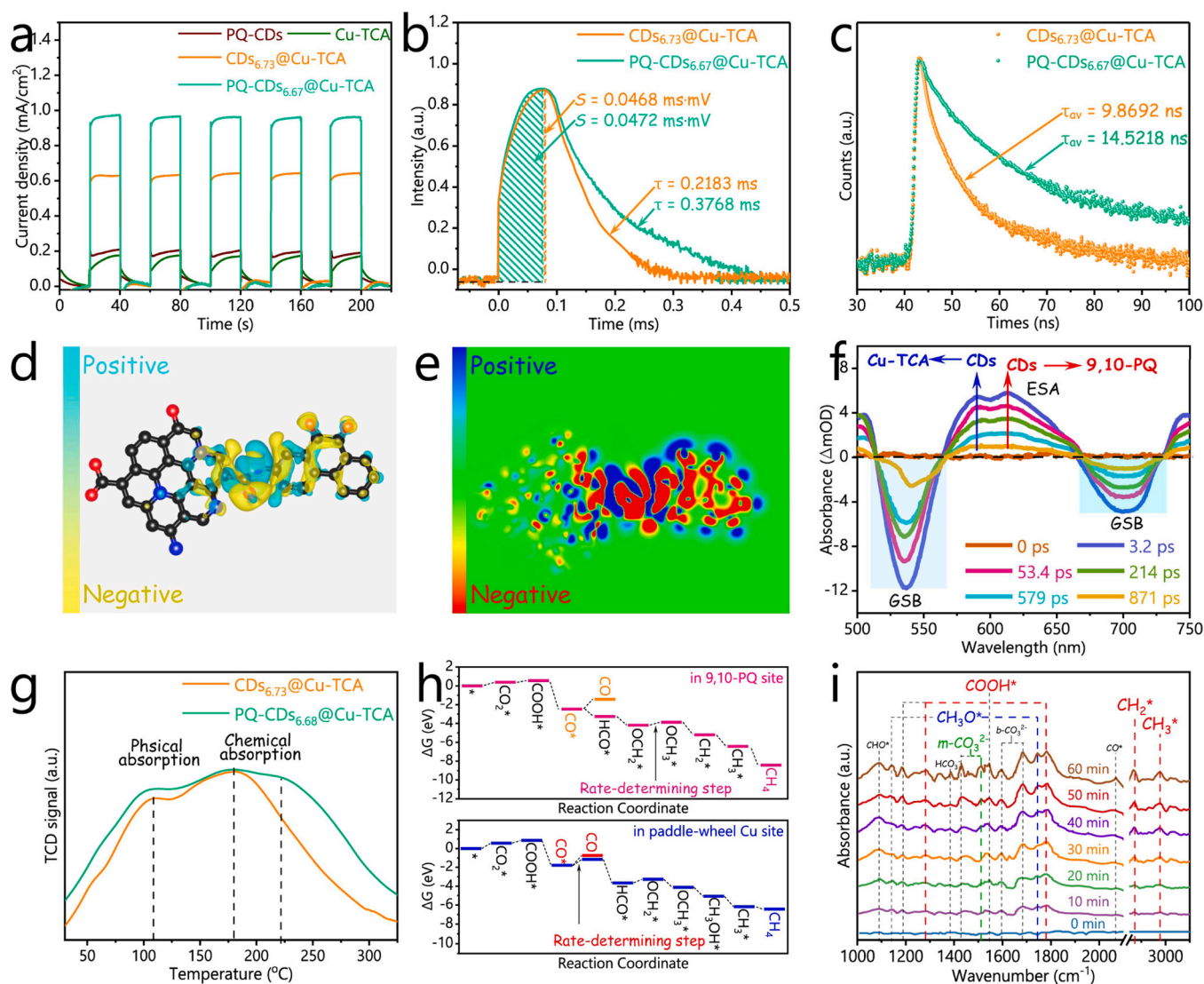Notably, the R_{ele} is significantly improved to 393.98 μmol·g^{-1}·h^{-1} after the introduction of 9,10-PQ structure, which is much higher than

Fig. 7. (a) The *i-t* curves of PQ-CDs, Cu-TCA, CDs$_{6.73}$@Cu-TCA and PQ-CDs$_{6.67}$@Cu-TCA. (b) TPV spectra, (c) TRPL spectra of CDs$_{6.73}$@Cu-TCA and PQ-CDs$_{6.67}$@Cu-TCA. (d) The 3D charge density differences of PQ-CDs. (e) The planar charge density diagram of cross-section for PQ-CDs. (f) TAS of PQ-CDs$_{6.67}$@Cu-TCA. (g) CO$_2$-TPD curves of CDs$_{6.73}$@Cu-TCA and PQ-CDs$_{6.67}$@Cu-TCA. (h) The calculated CO$_2$ reduction processes and corresponding Gibbs free energy in paddle-wheel Cu site and 9,10-PQ site of PQ-CDs$_{6.67}$@Cu-TCA. (i) *In-situ* DRIFTS of PQ-CDs$_{6.67}$@Cu-TCA.

that of CDs$_{6.73}$@Cu-TCA with the R_{ele} of 159.56 μmol·g^{-1}·h^{-1}. Based on similar chemical compositions, optical absorption properties and band structures of CDs$_{6.73}$@Cu-TCA and PQ-CDs$_{6.67}$@Cu-TCA heterojunctions, the significant differences in their R_{ele} have been focus on the charge separation capacities. As illustrated in Fig. 7a, PQ-CDs$_{6.67}$@Cu-TCA exhibits a highest average photocurrent density of 0.97 μA·cm^{-3}, which is 1.5-fold higher than that of CDs$_{6.73}$@Cu-TCA (0.63 μA·cm^{-3}). Obviously, the photogenerated charge separation ability of PQ-CDs$_{6.67}$@Cu-TCA is greatly enhanced. Meanwhile, the PL emission spectra of PQ-CDs and PQ-CDs$_{6.67}$@Cu-TCA at an excitation wavelength of 400 nm, exhibit their fluorescence signals with maximum emission wavelengths at 531.5 and 530.8 nm, respectively (Fig. S23). Relative to CDs$_{6.73}$@Cu-TCA, PQ-CDs$_{6.67}$@Cu-TCA exhibits a drastically reduced fluorescence intensity, suggesting that the electron-hole complexation phenomenon is greatly reduced in PQ-CDs$_{6.67}$@Cu-TCA. The TPV relaxation curves (Fig. 7b) indicate that the amount of maximum charge extraction for PQ-CDs$_{6.67}$@Cu-TCA (0.0472×10^{-6} V·s) is identical to that for CDs$_{6.73}$@Cu-TCA (0.0468×10^{-6} V·s). PQ-CDs$_{6.67}$@Cu-TCA shows a greater attenuation constant (τ, 0.3768 ms) than that of CDs$_{6.73}$@Cu-TCA (0.2182 ms), which confirms PQ-CDs$_{6.67}$@Cu-TCA has

a slower carriers recombination rate. TRPL decay spectroscopy indicates that the average PL lifetime of CDs$_{6.73}$@Cu-TCA is 9.8692 ns at 529 nm upon excitation at 400 nm, which is prolonged to 14.5218 ns for PQ-CDs$_{6.67}$@Cu-TCA (Fig. 7c). The results above fully demonstrate that the introduction of PQ greatly enhances the electron-hole separation ability and prolongs lifetime of photogenerated charge carriers of the pristine system.

To testify that photogenerated electrons can be transferred from CDs to 9,10-PQ sites, we calculate the charge density of the PQ-CDs through DFT (Fig. S24). As shown in Fig. 7d, the localized electron distribution can be clearly detected on PQ-CDs. Under the electron withdrawing effect of 9,10-PQ, the electrons generated on CDs are transferred to 9,10-PQ through amide bonds (-CONH-) and enriched at the carbonyl sites of 9,10-PQ (Fig. 7e). The DFT calculations demonstrate the feasibility of electron transfer from CDs to 9,10-PQ. To experimentally verify that 9,10-PQ serves as an electron acceptor within PQ-CDs$_{6.67}$@Cu-TCA, the samples are subjected to femtosecond transient absorption spectroscopy at a pump pulse of 400 nm and a probe of 500–750 nm (fs-TAS). As shown in Fig. 7f, two broad negative ground-state bleaches (GSB) at 514–565 nm and 665–731 nm can be corresponding to the intrinsic
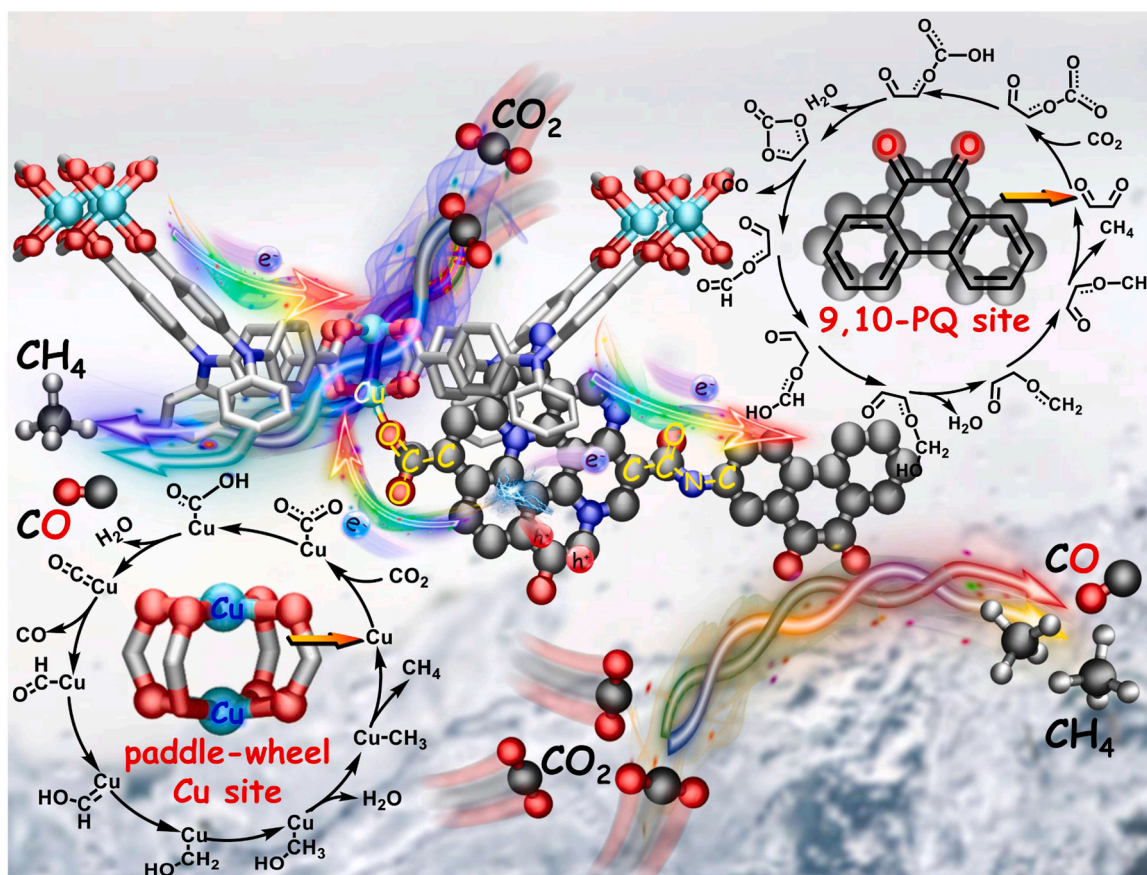
Fig. 8. The schematic diagram of PQ-CDs$_{6.67}$@Cu-TCA showing the dual-catalytic sites and parallel electron transfer pathways for photocatalytic CO_2 reduction.

excited-state of CDs and Cu-TCA, which is consistent with intrinsic band edges [45,46]. Notably, two excited state absorptions (ESA) with the peak values of 589 and 613 nm are observed in PQ-CDs$_{6.67}$@Cu-TCA, which demonstrates the existence of two different carrier transfer behaviors. By comparing with that of CDs$_{6.73}$@Cu-TCA (Fig. S25), it is reasonable to attribute the absorption at around 589 nm to the electron transfer from the excited state of CDs to Cu-TCA [47]. Therefore, the other absorption at around 613 nm demonstrated the existence of a new electron transition behavior in CDs, which may be related to the electron-withdrawing properties of PQ [48]. This result provides solid evidence that the electrons transfer *via* a new electron transfer pathway.

Subsequently, CO_2 temperature programmed desorption (CO_2-TPD) was performed to verify the ability of 9,10-PQ as a catalytic site. As reflected in Fig. 7g, PQ-CDs$_{6.67}$@Cu-TCA exhibits obvious chemical-absorption changes, a new chemical absorption peak appears at 223.4 °C compared with that of CDs$_{6.73}$@Cu-TCA (174.5 °C), which demonstrates the introducing 9,10-PQ group working as another CO_2 binding site. The possible reaction pathway and relative Gibbs free energy (ΔG) of intermediates on paddle-wheel Cu site and 9,10-PQ site in PQ-CDs$_{6.67}$@Cu-TCA are calculated. The calculation results show that the adsorption energies of CO_2 molecule on paddle-wheel Cu site and 9,10-PQ site are 0.39 and 0.56 eV, respectively, indicating that 9,10-PQ site have a stronger CO_2 capture ability. As depicted in Fig. 7h, it is in paddle-wheel Cu sites that, proton-coupled reduction of CO* to the HCO* intermediate is found to be highly exoergic ($\Delta G = 0.73$ eV) as compared to the endoergic desorption ($\Delta G = 1.06$ eV) of CO. There is a greater tendency to form CH_4 compared to form CO at the paddle-wheel Cu site. By contrast, the energy barriers of CO* to form CO and HCO* are 0.74 and −0.79 eV on 9,10-PQ site, respectively, which makes it easier for CO* to be proton-coupled to obtain HCO* compared to CO generation, further leading to the production of CH_4 products. This is also the

reason for the increase in CH_4 selectivity in PQ-CDs$_{6.67}$@Cu-TCA after the introduction of the 9,10-PQ sites. For paddle-wheel Cu site, the proton-coupled reduction follows the path HCO*→ OCH$_2$* → OCH$_3$* → CH$_3$OH* → CH$_3$* → CH$_4$. When in 9,10-PQ site, the proton-coupled reduction occurs in line with the different process of HCO*→ OCH$_2$* → OCH$_3$* → CH$_2$*→ CH$_3$* → CH$_4$.

In-situ DRIFTS was used to detect adsorbed intermediates on PQ-CDs$_{6.67}$@Cu-TCA during photocatalytic CO_2 reduction. As shown in Fig. 7i, after CO_2 and H_2O vapours are preabsorbed, the diffuse reflection peaks such as 1597 and 1683 cm^{-1} for b-CO_3^{2-}, 1428 and 1512 cm^{-1} for m-CO_3^{2-}, and 1387 cm^{-1} for bicarbonate species (HCO$_3$) are recorded, indicating strong CO_2 adsorption capacity onto dual-catalytic sites. Thereinto, the peak at 1512 cm^{-1} is attributed to characteristic binding m-CO_3^{2-} species on 9,10-PQ [49–51]. Upon photoirradiation, the peaks at 1134, 1159, 1187, 1376, 1441, 1537, 1552, 1676, 1792 and 2077 cm^{-1} are the intermediates of HCO*, CH$_3$O*, HCO$_3$*, COOH*, m-CO_3^{2-}, b-CO_3^{2-} and CO* detected on the Cu site, in agreement with CDs$_{6.73}$@Cu-TCA (Fig. 5i). Besides, the new peaks of COOH* (at 1280 and 1779 cm^{-1}), CH$_3$O* (at 1745 cm^{-1}) and CH$_3$* (2977 cm^{-1}) are ascribed to the intermediates adsorbed at the 9,10-PQ site [52,53]. Especially, the intermediate CH$_2$* at 2873 cm^{-1} are the crucial evidence for the new reduction process [54–56]. The result of *in-situ* DRIFTS evidences that 9, 10-PQ acts as the new CO_2 binding and catalytic sites in PQ-CDs$_{6.67}$@Cu-TCA.

Combination of fs-TAS, CO_2-TPD, DFT calculation and *in-situ* DRIFTS, 9,10-PQ group is the new electron acceptor and catalytic site in PQ-CDs$_{6.67}$@Cu-TCA. Upon irradiation, the photosensitive units TCA^{3-} ligands and CDs absorb light to make PQ-CDs$_{6.67}$@Cu-TCA reach its excited state, and subsequently the excited state transforms into a charge separation state, producing mobile electrons and holes. Besides modest LMCT in pristine Cu-TCA, the generated active electrons undergo two

dominant electron transferring pathways to arrive the Cu_2 and 9,10-PQ catalytic sites: 1) electrons transfer from PQ-CDs to paddlewheel Cu_2 sites; 2) electrons transferring from the main body of CDs to the 9,10-PQ sites. The paddle-wheel Cu_2 units and 9,10-PQ groups with enriched electrons adsorb and active CO_2, and the resulting intermediates rapidly couple protons from H_2O and undergo $2e^-/8e^-$ transfer to produce CO and CH_4. Meanwhile, the free holes in Cu-TCA are transferred from the VB of Cu-TCA to the VB of PQ-CDs, and then combine with the separated holes in PQ-CDs for TEA oxidation. The dual catalytic sites in the system relieve the recombination of photogenerated charge and maximumly utilize electrons, yielding an excellent photocatalytic CO_2 reduction performance (Fig. 8).

4. Conclusion

In summary, PQ-CDs$_{6.67}$@Cu-TCA with dual catalytic sites has been fabricated by a "building-bottle-around-ship" strategy and served as efficient photocatalyst toward the overall conversion of CO_2 to CH_4 and CO. PQ-CDs$_{6.67}$@Cu-TCA exhibited an excellent photocatalytic performance with R_{ele} of 393.98 $\mu mol \cdot g^{-1} \cdot h^{-1}$, R_{CH4} of 44.43 $\mu mol \cdot g^{-1} \cdot h^{-1}$ and S_{CH4} of 90.22%. The outstanding activity is attributed to combination of the dual catalytic sites, the paddle-wheel Cu_2 unit and the PQ group, and the parallel electron pathways in PQ-CDs$_{6.67}$@Cu-TCA system. This work integrates the electron-hole separation and recombination in CDs@MOF photocatalysts to maximise the utilization of CDs-supplied electrons, providing insights into the design of high-performance MOF-based photocatalysts.

CRediT authorship contribution statement

Ma Huiyang: Writing – original draft, Methodology, Investigation, Formal analysis. **Wang Tianyu:** Writing – review & editing, Visualization, Validation, Investigation, Formal analysis, Conceptualization. **Xu Yifan:** Methodology, Formal analysis. **Shi Weiliang:** Data curation. **Ma Ren:** Investigation, Formal analysis. **Xia Zhengqiang:** Methodology, Writing – review & editing, Resources, Visualization, Project administration, Funding acquisition, Conceptualization, Investigation. **Yang Qi:** Resources, Project administration. **Xie Gang:** Writing – review & editing, Supervision, Resources. **Chen Sanping:** Writing – review & editing, Visualization, Resources, Investigation, Funding acquisition.

Declaration of Competing Interest

The authors declare that they have no known competing financial interests or personal relationships that could have appeared to influence the work reported in this paper.

Data availability

Data will be made available on request.

Appendix A. Supporting information

Supplementary data associated with this article can be found in the online version at doi:10.1016/j.apcatb.2024.123857.

References

[1] X. Li, J. Zhang, Y. Huo, K. Dai, S. Li, S. Chen, Two-dimensional sulfur- and chlorine-codoped g-C_3N_4/CdSe-amine heterostructures nanocomposite with effective interfacial charge transfer and mechanism insight, Appl. Catal., B 280 (2021) 119452, https://doi.org/10.1016/j.apcatb.2020.119452.

[2] Z. Zhao, Z. Wang, J. Zhang, C. Shao, K. Dai, K. Fan, C. Liang, Interfacial chemical bond and oxygen vacancy-enhanced In_2O_3/CdSe-DETA S-scheme heterojunction for photocatalytic CO_2 conversion, Adv. Funct. Mater. 33 (2023) 2214470, https://doi.org/10.1002/adfm.202214470.

[3] L. Liu, Z. Wang, J. Zhang, O. Ruzimuradov, K. Dai, J. Low, Tunable interfacial charge transfer in a 2D–2D composite for efficient visible-light-driven CO_2 conversion, Adv. Mater. 35 (2023) 2300643, https://doi.org/10.1002/adma.202300643.

[4] J. Wei, Q. Ge, R. Yao, Z. Wen, C. Fang, L. Guo, H. Xu, J. Sun, Directly converting CO_2 into a gasoline fuel, Nat. Commun. 8 (2017) 15174, https://doi.org/10.1038/ncomms15174.

[5] Y. Fu, D. Sun, Y. Chen, R. Huang, Z. Ding, X. Fu, Z. Li, An amine-functionalized titanium metal–organic framework photocatalyst with visible-light-induced activity for CO_2 reduction, Angew. Chem. Int. Ed. 51 (2012) 3364–3367, https://doi.org/10.1002/anie.201108357.

[6] D. Sun, Y. Fu, W. Liu, L. Ye, D. Wang, L. Yang, X. Fu, Z. Li, Studies on photocatalytic CO_2 reduction over NH₂-Uio-66(Zr) and its derivatives: towards a better understanding of photocatalysis on metal–organic frameworks, Chem. - Eur. J. 19 (2013) 14279–14285, https://doi.org/10.1002/chem.201301728.

[7] D. Wang, R. Huang, W. Liu, D. Sun, Z. Li, Fe-based MOFs for photocatalytic CO_2 reduction: role of coordination unsaturated sites and dual excitation pathways, ACS Catal. 4 (2014) 4254–4260, https://doi.org/10.1021/cs501169t.

[8] H. Furukawa, K.E. Cordova, M. O'Keeffe, O.M. Yaghi, The chemistry and applications of metal-organic frameworks, Science 341 (2013) 1230444, https://doi.org/10.1126/science.1230444.

[9] N. Kolobov, M.G. Goesten, J. Gascon, Metal–organic frameworks: molecules or semiconductors in photocatalysis, Angew. Chem. Int. Ed. 60 (2021) 26038–26052, https://doi.org/10.1002/anie.202106342.

[10] K. Sun, Y. Qian, H.-L. Jiang, Metal-organic frameworks for photocatalytic water splitting and CO_2 reduction, Angew. Chem. Int. Ed. 62 (2023) e202217565, https://doi.org/10.1002/anie.202217565.

[11] S. Li, K. Ji, M. Zhang, C. He, J. Wang, Z. Li, Boosting the photocatalytic CO_2 reduction of metal–organic frameworks by encapsulating carbon dots, Nanoscale 12 (2020) 9533–9540, https://doi.org/10.1039/D0NR01696A.

[12] Z. Liang, C. Qu, W. Guo, R. Zou, Q. Xu, Pristine metal–organic frameworks and their composites for energy storage and conversion, Adv. Mater. 30 (2018) 1702891, https://doi.org/10.1002/adma.201702891.

[13] L. Sun, M.G. Campbell, M. Dincǎ, Electrically conductive porous metal–organic frameworks, Angew. Chem. Int. Ed. 55 (2016) 3566–3579, https://doi.org/10.1002/anie.201506219.

[14] E.M. Johnson, S. Ilic, A.J. Morris, Design strategies for enhanced conductivity in metal–organic frameworks, ACS Cent. Sci. 7 (2021) 445–453, https://doi.org/10.1021/acscentsci.1c00047.

[15] K. Guo, I. Hussain, Ga Jie, Y. Fu, F. Zhang, W. Zhu, Strategies for improving the photocatalytic performance of metal-organic frameworks for CO_2 reduction: a review, J. Environ. Sci. 125 (2023) 290–308, https://doi.org/10.1016/j.jes.2022.01.005.

[16] X.-W. Liu, T.-J. Sun, J.-L. Hu, S.-D. Wang, Composites of metal–organic frameworks and carbon-based materials: preparations, functionalities and applications, J. Mater. Chem. A 4 (2016) 3584–3616, https://doi.org/10.1039/C5TA09924B.

[17] Z. Xia, X. Jia, X. Ge, C. Ren, Q. Yang, J. Hu, Z. Chen, J. Han, G. Xie, S. Chen, S. Gao, Tailoring electronic structure and size of ultrastable metalated metal–organic frameworks with enhanced electroconductivity for high-performance supercapacitors, Angew. Chem. Int. Ed. 60 (2021) 10228–10238, https://doi.org/10.1002/anie.202100123.

[18] L. Liu, A. Corma, Confining isolated atoms and clusters in crystalline porous materials for catalysis, Nat. Rev. Mater. 6 (2021) 244–263, https://doi.org/10.1038/s41578-020-00250-3.

[19] L. Zeng, X. Guo, C. He, C. Duan, Metal–organic frameworks: versatile materials for heterogeneous photocatalysis, ACS Catal. 6 (2016) 7935–7947, https://doi.org/10.1021/acscatal.6b02228.

[20] L. Đorđević, F. Arcudi, M. Cacioppo, M. Prato, A multifunctional chemical toolbox to engineer carbon dots for biomedical and energy applications, Nat. Nanotechnol. 17 (2022) 112–130, https://doi.org/10.1038/s41565-021-01051-7.

[21] R. Wang, K.-Q. Lu, Z.-R. Tang, Y.-J. Xu, Recent progress in carbon quantum dots: synthesis, properties and applications in photocatalysis, J. Mater. Chem. A 5 (2017) 3717–3734, https://doi.org/10.1039/C6TA08660H.

[22] D. Saini, A.K. Garg, C. Dalal, S.R. Anand, S.K. Sonkar, A.K. Sonker, G. Westman, Visible-light-promoted photocatalytic applications of carbon dots: a review, ACS Appl. Nano Mater. 5 (2022) 3087–3109, https://doi.org/10.1021/acsanm.1c04142.

[23] J. Bao, J. Zhang, Y. Muhammad, H. Wei, R. Wang, G. Fang, Z. Zhao, Z. Zhao, Oriented anchoring of NCQD on citric acid defective cluster of NH₂-MIL-88B(Fe) for the efficient removal of tetracycline via photo-Fenton catalysis, Chem. Eng. J. 456 (2023) 141063, https://doi.org/10.1016/j.cej.2022.141063.

[24] P.M. Stanley, J. Haimerl, N.B. Shustova, R.A. Fischer, J. Warnan, Merging molecular catalysts and metal–organic frameworks for photocatalytic fuel production, Nat. Chem. 14 (2022) 1342–1356, https://doi.org/10.1038/s41557-022-01093-x.

[25] C.H. Sharp, B.C. Bukowski, H. Li, E.M. Johnson, S. Ilic, A.J. Morris, D. Gersappe, R.Q. Snurr, J.R. Morris, Nanoconfinement and mass transport in metal–organic frameworks, Chem. Soc. Rev. 50 (2021) 11530–11558, https://doi.org/10.1039/D1CS00558H.

[26] B.A. Johnson, A.M. Beiler, B.D. McCarthy, S. Ott, Transport phenomena: challenges and opportunities for molecular catalysis in metal–organic frameworks, J. Am. Chem. Soc. 142 (2020) 11941–11956, https://doi.org/10.1021/jacs.0c02899.

[27] J. Liu, T.A. Goetjen, Q. Wang, J.G. Knapp, M.C. Wasson, Y. Yang, Z.H. Syed, M. Delferro, J.M. Notestein, O.K. Farha, J.T. Hupp, MOF-enabled confinement and related effects for chemical catalyst presentation and utilization, Chem. Soc. Rev. 51 (2022) 1045–1097, https://doi.org/10.1039/D1CS00968K.

[28] W. Zhang, W. Huang, B. Wu, J. Yang, J. Jin, S. Zhang, Excitonic effect in MOFs-mediated photocatalysis: Phenomenon, characterization techniques and regulation strategies, Coord. Chem. Rev. 491 (2023) 215235, https://doi.org/10.1016/j.ccr.2023.215235.

[29] Z. Tian, X. Zhang, D. Li, D. Zhou, P. Jing, D. Shen, S. Qu, R. Zboril, A.L. Rogach, Full-color inorganic carbon dot phosphors for white-light-emitting diodes, Adv. Opt. Mater. 5 (2017) 1700416, https://doi.org/10.1002/adom.201700416.

[30] X. Miao, D. Qu, D. Yang, B. Nie, Y. Zhao, H. Fan, Z. Sun, Synthesis of carbon dots with multiple color emission by controlled graphitization and surface functionalization, Adv. Mater. 30 (2018) 1704740, https://doi.org/10.1002/adma.201704740.

[31] S. Feng, J. Wang, Z. Tong, H.-Y. Qu, Metal-organic framework thin films with diverse redox-active/inactive components for enhanced optical modulation and coloration efficiency, Chem. Eng. J. 442 (2022) 136158, https://doi.org/10.1016/j.cej.2022.136158.

[32] H. He, J. Guo, J. Zhao, J. Xu, C. Zhao, Z. Gao, Y.-Y. Song, Engineering CuMOF in TiO₂ nanochannels as flexible gas sensor for high-performance NO detection at room temperature, ACS Sens 7 (2022) 2750–2758, https://doi.org/10.1021/acssensors.2c01318.

[33] M. Karimi, S. Sadeghi, H. Mohebali, Z. Azarkhosh, V. Safarifard, A. Mahjoub, A. Heydari, Fluorinated solvent-assisted photocatalytic aerobic oxidative amidation of alcohols via visible-light-mediated HKUST-1/Cs-POMoW catalysis, N. J. Chem. 45 (2021) 14024–14035, https://doi.org/10.1039/D1NJ02401A.

[34] J. Tauc, R. Grigorovici, A. Vancu, Optical properties and electronic structure of amorphous germanium, Phys. Status Solidi B 15 (1966) 627–637, https://doi.org/10.1002/pssb.19660150224.

[35] Z. Sun, N. Talreja, H. Tao, J. Texter, M. Muhler, J. Strunk, J. Chen, Catalysis of carbon dioxide photoreduction on nanosheets: fundamentals and challenges, Angew. Chem. Int. Ed. 57 (2018) 7610–7627, https://doi.org/10.1002/anie.201710509.

[36] L. Jiang, H. Ding, M. Xu, X. Hu, S. Li, M. Zhang, Q. Zhang, Q. Wang, S. Lu, Y. Tian, H. Bi, UV–Vis–NIR full-range responsive carbon dots with large multiphoton absorption cross sections and deep-red fluorescence at nucleoli and in vivo, Small 16 (2020) 2000680, https://doi.org/10.1002/smll.202000680.

[37] L. Tang, L. Ai, Z. Song, L. Sui, J. Yu, X. Yang, H. Song, B. Zhang, Y. Hu, Y. Zhang, Y. Tian, S. Lu, Acid-triggered aggregation of carbon dots shifted their emission to give unexpected deep-red lasing, Adv. Funct. Mater. 33 (2023) 2303363, https://doi.org/10.1002/adfm.202303363.

[38] D. Samanta, M. Kumar, S. Singh, P. Verma, K.K. Kar, T.K. Maji, M.K. Ghorai, Triphenylamine and terpyridine–zinc(ii) complex based donor–acceptor soft hybrid as a visible light-driven hydrogen evolution photocatalyst, J. Mater. Chem. A 8 (2020) 21968–21972, https://doi.org/10.1039/D0TA02318C.

[39] H. Deng, S. Grunder, K.E. Cordova, C. Valente, H. Furukawa, M. Hmadeh, F. Gándara, A.C. Whalley, Z. Liu, S. Asahina, H. Kazumori, M. O'Keeffe, O. Terasaki, J.F. Stoddart, O.M. Yaghi, Large-pore apertures in a series of metal-organic frameworks, Science 336 (2012) 1018–1023, https://doi.org/10.1126/science.1220131.

[40] S. Barman, A. Singh, F.A. Rahimi, T.K. Maji, Metal-free catalysis: a redox-active donor–acceptor conjugated microporous polymer for selective visible-light-driven CO₂ reduction to CH₄, J. Am. Chem. Soc. 143 (2021) 16284–16292, https://doi.org/10.1021/jacs.1c07916.

[41] P. Liu, Z. Huang, X. Gao, X. Hong, J. Zhu, G. Wang, Y. Wu, J. Zeng, X. Zheng, Synergy between palladium single atoms and nanoparticles via hydrogen spillover

for enhancing CO₂ photoreduction to CH₄, Adv. Mater. 34 (2022) 2200057, https://doi.org/10.1002/adma.202200057.

[42] C. Ding, X. Lu, B. Tao, L. Yang, X. Xu, L. Tang, H. Chi, Y. Yang, D.M. Meira, L. Wang, X. Zhu, S. Li, Y. Zhou, Z. Zou, Interlayer spacing regulation by single-atom indium$^{\delta+}$–N₄ on carbon nitride for boosting CO₂/CO photo-conversion, Adv. Funct. Mater. 33 (2023) 2302824, https://doi.org/10.1002/adfm.202302824.

[43] Y. Zou, K. Xiao, Q. Qin, J.-W. Shi, T. Heil, Y. Markushyna, L. Jiang, M. Antonietti, A. Savateev, Enhanced organic photocatalysis in confined flow through a carbon nitride nanotube membrane with conversions in the millisecond regime, ACS Nano 15 (2021) 6551–6561, https://doi.org/10.1021/acsnano.0c09661.

[44] Y.-F. Miao, R.-T. Guo, J.-W. Gu, Y.-Z. Liu, G.-L. Wu, C.-P. Duan, W.-G. Pan, Oxygen vacancy-rich BiO₂₋ₓ: super-active co-catalyst on g-C₃N₄ for efficient visible-light photocatalytic CO₂ reduction, J. CO2 Util. 44 (2021) 101377, https://doi.org/10.1016/j.jcou.2020.101377.

[45] Y. Li, S. Yu, J. Xiang, F. Zhang, A. Jiang, Y. Duan, C. Tang, Y. Cao, H. Guo, Y. Zhou, Revealing the importance of hole transfer: boosting photocatalytic hydrogen evolution by delicate modulation of photogenerated holes, ACS Catal. 13 (2023) 8281–8292, https://doi.org/10.1021/acscatal.3c01210.

[46] Y. He, Y. Zhao, X. Wang, Z. Liu, Y. Yu, L. Li, Multiple heteroatom-hydrogen bonds bridging electron transport in covalent organic framework-based supramolecular system for photoreduction of CO₂, Angew. Chem. Int. Ed. 62 (2023) e202307160, https://doi.org/10.1002/anie.202307160.

[47] Z. Ming, T. Zhang, W. Tian, J. Li, Z. Liu, R. Liu, Z. Liu, C. Duan, Dye–polyoxometalate coordination polymer as a photo-driven electron pump for photocatalytic radical coupling reactions, Chem. Commun. 57 (2021) 12812–12815, https://doi.org/10.1039/D1CC04209B.

[48] J. Jing, J. Li, Y. Su, Y. Zhu, Non-covalently linked donor-acceptor interaction enhancing photocatalytic hydrogen evolution from porphyrin assembly, Appl. Catal., B 324 (2023) 122284, https://doi.org/10.1016/j.apcatb.2022.122284.

[49] Y. Zhang, L. Cao, G. Bai, X. Lan, Engineering single Cu sites into covalent organic framework for selective photocatalytic CO₂ reduction, Small 19 (2023) 2300035, https://doi.org/10.1002/smll.202300035.

[50] L. Huang, S. Mo, X. Zhao, J. Zhou, X. Zhou, Y. Zhang, M. Fu, Y. Fan, Q. Xie, D. Ye, Y. Chen, Designing multi-layered MOF-on-MOF-transformed core double-shell FeSₓ@ZnS@CoSₓ heterojunction for enhanced CO₂ photoreduction with water vapor, Chem. Eng. J. 474 (2023) 145740, https://doi.org/10.1016/j.cej.2023.145740.

[51] B. Lei, W. Cui, P. Chen, L. Chen, J. Li, F. Dong, C–doping induced oxygen-vacancy in WO₃ nanosheets for CO₂ activation and photoreduction, ACS Catal. 12 (2022) 9670–9678, https://doi.org/10.1021/acscatal.2c02390.

[52] S. Yang, W. Hu, X. Zhang, P. He, B. Pattengale, C. Liu, M. Cendejas, I. Hermans, X. Zhang, J. Zhang, J. Huang, 2D covalent organic frameworks as intrinsic photocatalysts for visible light-driven CO₂ reduction, J. Am. Chem. Soc. 140 (2018) 14614–14618, https://doi.org/10.1021/jacs.8b09705.

[53] X. Li, Y. Sun, J. Xu, Y. Shao, J. Wu, X. Xu, Y. Pan, H. Ju, J. Zhu, Y. Xie, Selective visible-light-driven photocatalytic CO₂ reduction to CH₄ mediated by atomically thin CuIn₅S₈ layers, Nat. Energy 4 (2019) 690–699, https://doi.org/10.1038/s41560-019-0431-1.

[54] K. Lei, D. Wang, L. Ye, M. Kou, Y. Deng, Z. Ma, L. Wang, Y. Kong, A metal-free donor–acceptor covalent organic framework photocatalyst for visible-light-driven reduction of CO₂ with H₂O, ChemSusChem 13 (2020) 1725–1729, https://doi.org/10.1002/cssc.201903545.

[55] L. Liang, X. Li, Y. Sun, Y. Tan, X. Jiao, H. Ju, Z. Qi, J. Zhu, Y. Xie, Infrared light-driven CO₂ overall splitting at room temperature, Joule 2 (2018) 1004–1016, https://doi.org/10.1016/j.joule.2018.02.019.

[56] Z. Jiang, H. Sun, T. Wang, B. Wang, W. Wei, H. Li, S. Yuan, T. An, H. Zhao, J. Yu, P. K. Wong, Nature-based catalyst for visible-light-driven photocatalytic CO₂ reduction, Energy Environ. Sci. 11 (2018) 2382–2389, https://doi.org/10.1039/C8EE01781F.